DOI: 10.1002/ ((please add manuscript number))
Article type: Full Paper

High-Rate and Ultralong Cycle-Life Potassium Ion Batteries Enabled by In-Situ Engineering of Yolk-Shell FeS_2@C Structure on Graphene Matrix

Yi Zhao, Jiajie Zhu, Samuel Jun Hoong Ong, Qianqian Yao, Xiuling Shi, Kun Hou, Zhichuan J. Xu, Lunhui Guan**

Dr. Y. Zhao, Ms. Q. Q. Yao, Ms. X. L. Shi, Dr. K. Hou, Prof. L. H. Guan
CAS Key Laboratory of Design and Assembly of Functional Nanostructures, Fujian Key Laboratory of Nanomaterials, Fujian Institute of Research on the Structure of Matter, Chinese Academy of Sciences, Fuzhou 350108, China.
E-mail: guanlh@fjirsm.ac.cn

Dr. J. J. Zhu
College of Materials Science and Engineering, Shenzhen University, Nanhai Ave 3688, ShenZhen, Guangdong 518060, China

Dr. Y. Zhao, Mr. S. J. H. Ong, Prof. Z. Xu
School of Materials Science and Engineering, Nanyang Technological University, Singapore 639798, Singapore.
E-mail: xuzc@ntu.edu.sg

Mr. S. J. H. Ong, Prof. Z. Xu
Singapore-HUJ Alliance for Research and Enterprise (SHARE), Nanomaterials for Energy and Energy-Water Nexus (NEW), Campus for Research Excellence and Technological Enterprise (CREATE), Singapore 138602
Energy Research Institute@NTU, Nanyang Technological University, 50 Nanyang Drive, Singapore, Singapore 639798, Singapore
Solar Fuels Lab, Nanyang Technological University, 50 Nanyang Drive, Singapore, Singapore 639798, Singapore

Keywords: yolk-shell structure; FeS_2 anode; graphene; carbon coating; potassium-ion batteries

Abstract

The potassium-ion battery (PIB) represents a promising alternative to the lithium-ion battery for large-scale energy storage owing to the abundance and low cost of potassium. The lack of high performance anode materials is one of bottlenecks for its success. The main challenge is the structural degradation caused by the huge volume expansion from insertion/extraction of potassium ions which are much larger than their lithium counterparts. Here, we tackle this challenge by in-situ engineering of a yolk-shell FeS_2@C structure on a graphene matrix. The yolk-shell structure provides interior void space for volume expansion and prevent the aggregation of FeS_2. The conductive graphene matrix further enhances the charge transport within the composite. The PIB fabricated using this anode delivers high capacity, good rate capability (203 mA h g^{-1} at 10 A g^{-1}), and remarkable long-term stability up to 1500 cycles at high rates. The performance is superior to most anode materials reported to date for PIBs. Further in-depth characterizations and density functional theory calculations reveal that the material displays reversible intercalation/deintercalation and conversion reactions during cycles, as well as the low diffusion energy barriers for the intercalation process. This work provides a new avenue to allow the proliferation of PIB anodes.

1. Introduction

Lithium-ion batteries (LIBs) as a power source have been widely applied in consumer electronics and electrical vehicles, and are expected to be a promising candidate for emerging smart grid technology in the near future. Nevertheless, the scarcity and uneven distribution of

lithium resources hamper its further development. In pursuit of alternatives to LIBs for large-scale applications, sodium-ion batteries (SIBs) and potassium-ion batteries (PIBs) have great potential, owing to the low cost and high abundance of Na (2.36 wt%) and K (2.09 wt%) in the Earth's crust, as well as its similar chemical properties to those of lithium.[1-5] Much work so far has focused on SIBs, and significant progress has been achieved in the past few years.[6-8] On the contrary, the development of PIBs is still in its infancy, probably due to the larger ionic radius of K^+ (1.38 Å) than those of Na^+ (1.02 Å) and Li^+ (0.76 Å).[9] However, PIBs possess several advantages compared with SIBs, such as the more negative standard potential of K^+/K (-2.93 V vs. SHE, compared with -2.71 V for Na^+/Na), reversible intercalation/deintercalation of K^+ in graphite (theoretical capacity of 279 mA h g^{-1}), and fast ionic conductivity of K^+ in liquid electrolyte.[10-12] These properties of PIBs offer exciting opportunities to achieve low-cost batteries with high energy density and good rate performance. Nevertheless, it remains challenging to fabricate suitable electrode materials, which can host the large size of K^+ ions and accommodate the huge volume fluctuation during cycles.

Until now, only a few materials have been evaluated as anode materials for PIBs, including graphite,[13, 14] soft/hard carbons,[15-17] graphene,[18] heteroatom-doped carbons,[19-21] alloying-type metals,[22-24] as well as conversion-type metal oxide/sulfides.[25-29] Normally, carbon-based anodes can deliver good cycling stability, but with low potassium storage capacity of below 300 mA h g^{-1}. Although the alloying/conversion-based anodes exhibit high theoretical capacities, their large volume variations during cycles result in poor cyclic performance. It is well established that the integration of a carbon matrix and a high-capacity anode material is an efficient strategy to enhance the electrochemical performance.[30-32] Graphene in particular, with its excellent physical and chemical properties, has been widely adopted to support active materials, which can effectively improve electrical conductivity and buffer volume changes during cycles.[33-36] For instance, Lakshmi et al. reported a SnS_2-graphene composite as PIB

anode, which can maintain a capacity of 250 mA h g^{-1} after 30 cycles.[37] Another graphene-CoS composite was able to retain a high capacity of 310 mA h g^{-1} after 100 cycles at 500 mA g^{-1}.[38] However, the huge volume variation during cycles would cause the inevitable agglomeration and pulverization of active materials on the graphene surface, resulting in unsatisfactory cycling stability. Drawing on successful experience from LIBs and SIBs, rational microstructure design elements, including structural modification of the active material and addition of a protection layer, play critical roles in further enhancing the electrochemical performance of graphene-based composites.[30, 35, 39] Moreover, pyrite (FeS_2), which uses a conversion-type reaction mechanism, showed a high theoretical specific capacity of 894 mA h g^{-1}, and displayed superior lithium and sodium storage properties.[40] So far, no systematic study concerning FeS_2 anodes for PIBs has been published. Therefore, combining high capacity FeS_2 with a graphene matrix using a rational microstructure design would be a promising method of achieving high-performance PIB anodes.

Herein, we have systematically investigated the potassium storage performance of FeS_2-graphene composites using various microstructures. As anode materials for PIBs, pure FeS_2 and G@FeS_2 electrodes showed fast capacity fading after the initial cycles. The addition of a carbon coating in G@FeS_2@C composite can enhance capacity retention in the first 20 cycles, but results in low coulumbic efficiency and rapid capacity decay in the following cycles. Through rational engineering of yolk-shell FeS_2@C structures on a graphene matrix, an as-prepared G@Y-S FeS_2@C composite can offer good electrical conductivity and large interior void space for the volume accommodation of FeS_2. Hence, it can deliver a high initial charge capacity of 489 mA h g^{-1} at 300 mA g^{-1}, which is sustained at 308 and 270 mA h g^{-1} after 100 and 1000 cycles, respectively. At high rates of 10 and 15 A g^{-1}, it still maintained capacities of 203 and 166 mA h g^{-1}, respectively. A remarkable long-term cycling of up to 1500 cycles was also observed at high current densities of 2 and 5 A g^{-1}. Impressively, the rate capabilities and cycling retention of G@Y-S FeS_2@C anode were much better than the Y-S FeS_2@C

composite. Moreover, the potassium storage mechanism of FeS_2 and the morphology evolution during cycles were systematically explored through electrochemical tests, *ex-situ* XRD, HRTEM, SEM characterizations, and theoretical calculations.

2. Results and Discussion

Figure 1a illustrates the formation process of G@Y-S FeS_2@C composite. Firstly, graphene oxide (GO) was covered with FeOOH nanorods through a facile hydrolysis of $FeCl_3$.[41] Then, the GO@FeOOH composite was coated with a resorcinol-formaldehyde (RF) resin layer, followed by a carbonization process at 550 ^oC for 2h under Ar.[42] Subsequently, the as-prepared G@Fe_3O_4@C sample was etched with 1 M HCl solution for 8h to generate interior void space between Fe_3O_4 and carbon coating.[43] Finally, a sulfuration treatment was carried out on G@Y-S Fe_3O_4@C using sulfur powder to synthesize G@Y-S FeS_2@C composite. Figure 1b compares the potassiation behaviors of various graphene-FeS_2 composites as anode materials for PIBs. For a graphene-FeS_2 electrode, the huge volume variation of FeS_2 would cause aggregation and pulverization upon repeated cycling, leading to the exfoliation of active material from graphene and fast capacity fading. The addition of a protective carbon coating on G@FeS_2@C composite could alleviate these problems, but the huge volume fluctuation would eventually result in the cracking of the carbon shell with inevitable pulverization and exfoliation of FeS_2 after long cycles. Thus, our rationally designed G@Y-S FeS_2@C composite displays several advantages: 1) the yolk-shell FeS_2@C structure can provide enough interior void space to fully accommodate the volume variation of FeS_2 during cycles without cracking of carbon coating. 2) The rigid carbon shell can prevent the agglomeration of FeS_2 during cycles, and facilitate the growth of a stable solid-electrolyte interphase (SEI) layer. 3) The graphene matrix and thin carbon coating shell can enhance electrical conductivity, and facilitate ion transportation across the carbon networks, benefiting charge transport kinetics.

Figure 2a-b displays the morphology evolution of G@Fe_3O_4@C composite before and after HCl etching. Seen from Figure 2a, Fe_3O_4 nanorods were homogeneously dispersed on graphene matrix without aggregation, coinciding with that observed in GO@FeOOH composite (Figure S1). The compact carbon coating layers on the surface of Fe_3O_4 particles were further disclosed in the TEM images (Figure S2). The thickness of the carbon shell was around 2-4 nm. After etching with 1M HCl for 8h, the particle size of Fe_3O_4 significantly decreased, as confirmed in Figure 2b and S2. The interior void space between Fe_3O_4 core and carbon shell can be clearly observed, demonstrating the formation of yolk-shell Fe_3O_4@C structure on graphene matrix. The HRTEM images in Figure S2 revealed the interlayer spacing of 0.24 nm, which can be ascribed to the (222) planes of Fe_3O_4. In Figure 2c, the diffraction peaks of G@Fe_3O_4@C and G@Y-S Fe_3O_4@C composites can be well assigned to the face-centered-cubic Fe_3O_4 (JCPDS No. 19-0629). The diffraction peaks of G@Y-S Fe_3O_4@C were broader and lower in intensity, indicating the smaller particle size in the yolk-shell structure, consistent with the observation from SEM and TEM. Moreover, by further increasing the etching time, Fe_3O_4 particles can be completely removed to generate hollow carbon particles on graphene substrate (G@hollow carbon), as shown in Figure S3.

Figure 2d-g shows the morphology and structure of G@Y-S FeS_2@C composite through SEM and TEM characterizations. As can be seen, the structure of G@Y-S Fe_3O_4@C was perfectly inherited even after sulfuration treatment. We can clearly observe that yolk-shell FeS_2@C composites with large interior void space were uniformly distributed on the graphene matrix. The particle size of FeS_2 was around 20-60 nm (Figure S4). A lattice spacing of 0.24 nm, corresponding to the (210) plane of pyrite FeS_2, was also identified in the high-resolution TEM (HRTEM) image (Figure 2h). The selected-area electron diffraction (SAED) pattern presents distinct diffraction rings, which can be indexed to the (200), (211), (220), and (311) planes of polycrystalline FeS_2. For G@FeS_2@C composite, irregular FeS_2 particles (size around 60-150 nm) covered with thin carbon shells were anchored on graphene

matrix (Figure S5). No empty space was found between FeS_2 and carbon coating in this composite. The XRD patterns (Figure 2i and S5) further confirmed the formation of pyrite FeS_2 (JCPDS No. 42-1340) after sulfuration treatment. As seen in Figure S6-7, both of the pure FeS_2 and G@FeS_2 composite exhibited large aggregated FeS_2 particles after sulfuration treatment. Besides, Y-S FeS_2@C composites (Figure S8-9) were also synthesized through a similar process to that of G@Y-S FeS_2@C composite except without the addition of GO.

Nitrogen adsorption-desorption isotherms were performed to analyse the surface area and porosity properties of the samples before and after sulfuration treatment. As seen from Figure S10, the HCl etching process enabled an increase of total pore volume from 0.81 $cm^3\ g^{-1}$ to 1.96 $cm^3\ g^{-1}$, demonstrating the generation of large interior void space in G@Y-S Fe_3O_4@C composite. After sulfuration, as-prepared G@Y-S FeS_2@C composite exhibits a high surface area of 537.8 $m^2\ g^{-1}$ and a large pore volume of 1.54 $cm^3\ g^{-1}$. The pore size distribution in Figure S10 shows that there are abundant mesopores at 2.2 and 3.75 nm in size, as well as a broad overall pore distribution of 5 to 30 nm. Therefore, this composite can provide large electrolyte/electrode contact area, and enough empty room for the volume variation of FeS_2 during cycles, potentially leading to superior potassium storage performance.[44-46] The weight contents of Fe_3O_4 and FeS_2 in these composites were determined with thermogravimetric analysis (TGA) in air (Figure S11). Given that the final product is Fe_2O_3, the HCl etching decreased the content of Fe_3O_4 from 77 wt% in G@Fe_3O_4@C composite to 32 wt% in G@Y-S Fe_3O_4@C composite. After sulfuration treatment, the loading ratios of FeS_2 were calculated to be 83 and 39 wt% for G@FeS_2@C and G@Y-S FeS_2@C composites, respectively.

The potassium storage mechanism of FeS_2 anode was investigated through cyclic voltammetry (CV), discharge/charge profiles, *ex-situ* XRD, and *ex-situ* HRTEM characterizations. **Figure 3**a shows the CV curves of pure FeS_2 electrode for the first three cycles at a scan rate of 0.2 mV s^{-1} between 0.05 and 2.8 V (*vs.* K^+/K). In the initial cathodic scan, there are two peaks at 1.0 V and 0.3 V. The large peak at 1.0 V can be ascribed to the

potassium intercalation to form K_xFeS_2 (x<2).[47] The initial discharge profile in Figure 3b also exhibited a plateau around 1.1 V related with the formation of K_xFeS_2. The broad peak near 0.3 V was assigned to the conversion reaction to form Fe and K_2S, as well as the formation of an irreversible SEI layer.[48] During the initial anodic scan, the broad peaks near 0.95, 1.5 and 2.5 V could be attributed to the conversion process from metallic Fe to K_xFeS_2, and the further depotassiation of K^+ in K_xFeS_2 compound. In the following scans, the reversible cathodic/anodic pairs at higher voltages were ascribed to the K^+ intercalation and deintercalation process in K_xFeS_2. The redox peaks at lower voltages were related with the reversible conversion reaction between K_xFeS_2 and Fe + K_2S.[49-51] To further illuminate the reaction mechanism, *ex-situ* XRD measurements were performed on pure FeS_2 electrode at selected discharge and charge states. According to Figure 3c, the pristine electrode only exhibited the diffraction peaks of FeS_2. After initial discharge to 1.1 V (stage B), the peak intensities of the FeS_2 phase decreased and a small diffraction peak (~30.6º) of $KFeS_2$ phase appeared, indicating the potassium intercalation into FeS_2 to form K_xFeS_2. After discharging to 0.5 V (stage C), the peaks of FeS_2 and $KFeS_2$ totally disappeared, and new peaks of Fe located at 43º and 50º were found, demonstrating the occurrence of conversion reaction at low voltage. However, there were no diffraction peaks at discharge 0.05 V (stage D) and charge 1.8 V (stage E), probably due to the low crystallinity or very small particle size of reaction products, as well as the formation of a thick SEI film.[52] When initially charged to 2.8 V, obvious diffraction peaks corresponding to a $KFeS_2$ phase and a small peak of K_2S were observed, showing that the final charged product was K_xFeS_2 instead of pyrite.[53] The HRTEM image in Figure 3d shows lattice fringes with interlayer spacing of 0.21 nm, confirming the existence of metallic Fe after the cell is fully discharged to 0.05 V. After being fully charged to 2.8 V (Figure 3e), the interlayer spacing of 0.29 nm shown could be assigned to the (22-1) planes of $KFeS_2$, consistent with the *ex-situ* XRD result.

To further explore the possible intermediate phase and intercalation/deintercalation process, density functional theory (DFT) calculations were carried out.[54, 55] Three kinds of crystal structures were considered as possible intermediate phases induced by potassiation in FeS_2, namely FeS_2, $KFeS_2$, and $K_3(FeS_2)_2$ structures (Figure S12). FeS_2 was calculated to show negative voltages for K intercalation, reflecting instability, due to its compact structure (density: 5.05 g/cm^3). The reaction voltages for $KFeS_2$ (density: 2.68 g/cm^3) and $K_3(FeS_2)_2$ (density: 2.60 g/cm^3) based on the following reactions of $K+FeS_2 \rightarrow KFeS_2$, and $3K+2FeS_2 \rightarrow K_3(FeS_2)_2$ in the first cycle were calculated to be 1.53 V and 1.52 V, respectively, in comparison to the peak at 1.0 V in the initial cathodic CV scan. In combination with the observations from *ex-situ* XRD and HRTEM, we can conclude that FeS_2 first reacts with K^+ ions to form a $KFeS_2$ phase in the initial potassiation process. The intercalation/deintercalation reactions can occur in this structure for further potassiation and depotassiation. The voltages for K_xFeS_2 as a function of x are shown in Figure 3f. The average voltages were calculated to be 2.19 V for K_xFeS_2 ($0<x<1$), which may correspond to the redox pair at 1.7/2.5 V in Figure 3a. Further potassium intercalation into the compounds leads to an x value beyond the stoichiometric ratio ($1<x<2$) with average voltages of 1.0 V, in agreement with the redox pair at 0.8/1.5 V in the CV curves. The maximum x value in K_xFeS_2 compound can reach to 2.0 with theoretical potassium storage of 447 mA h g^{-1}, which is close to the specific capacity of FeS_2 anode above 1.0 V in the first discharge curve. On the basis of these results, the reaction mechanism of FeS_2 during potassiation/depotassiation processes is schematically illustrated in Figure 3g. In the initial potassiation process, FeS_2 first reacts with K^+ to form K_xFeS_2, followed with intercalation process to generate K_yFeS_2 ($x<y<2$). Upon further potassiation, the K_yFeS_2 breaks into metallic Fe and K_2S through conversion reaction. In the depotassiation process, metallic Fe is converted back to K_yFeS_2, and then further deintercalated to form K_xFeS_2 as the final product. Based on the reversible redox pairs in CV

curves and the calculation results, it can be concluded that FeS_2 anode displays reversible intercalation/deintercalation reaction and conversion reaction in the subsequent cycles.

Figure 4 displays the potassium storage performance of as-prepared FeS_2-based composites as PIB anodes. All the capacities were calculated based on the mass of whole composite. The initial three discharge-charge profiles of these electrodes at 300 mA g^{-1} were shown in Figure 4a and Figure S13. As can be seen, the G@Y-S FeS_2@C electrode delivered discharge and charge capacities of 1357 and 489 mA h g^{-1} in the first cycle, corresponding to an initial coulumbic efficiency of 36%. The electrode after initial cycle was characterized by *ex-situ* TEM (Figure S14), from which the yolk-shell structure of G@Y-S FeS_2@C composite can be observed and the large pores remained unblocked. Therefore, blocking these large pores can be excluded as the main reason for the large capacity loss during first cycle. Instead, similar to reported elsewhere,[15, 21, 38] such loss should be mainly ascribed to the formation of irreversible SEI film on the large electrode surface. In addition, the decomposition of electrolyte, the irreversible reaction between potassium ions and residual oxygen-containing functional groups from RF-derived carbon, as well as the dissolution of sulfur component may also contribute to the irreversible capacity loss during the first cycles.[48, 51] For G@FeS_2@C electrode, it showed an initial charge capacity of 451 mA h g^{-1} and a CE of 45.5%. Considering the higher initial charge capacity and lower weight content of FeS_2 in G@Y-S FeS_2@C composite than those of G@FeS_2@C, we can conclude that the small particle size and the interior void space can significantly enhance the electrochemical reaction kinetics of FeS_2. For pure FeS_2 and G@FeS_2 electrodes with large particle size, they only exhibited low initial charge capacities of 360 and 414 mA h g^{-1}, along with coulumbic efficiencies of 38% and 36%, respectively.

Figure 4b exhibits the cycling stability of these electrodes at 300 mA g^{-1}. Both FeS_2 and G@FeS_2 electrodes displayed fast capacity fading from initial cycles, and only retained low capacities of 12 and 20 mA h g^{-1} after 100 cycles, respectively. Such poor cyclability was due

to the large volume fluctuation of FeS_2 during the potassium insertion/extraction process, which resulted in severe aggregation and pulverization during cycles.[56] For G@FeS_2@C electrode with carbon coating protection, it can display good cycling retention in the initial cycles, and kept a high discharge capacity around 417 mA h g^{-1} at 20th cycle. However, the CE sharply decreased from the 20th cycle onwards and the discharge capacity quickly decayed after the 30th cycle. As seen from Figure S13, the average CE of the G@FeS_2@C electrode between 20 to 50 cycles was only ~82.3%. Such a low CE was attributed to the cracking of carbon coating layer, which exposed new fresh active material to increase side reaction and SEI film formation between electrode and electrolyte. Furthermore, the broken carbon layer cannot prevent the FeS_2 particles from aggregating, thus resulting in a low capacity of 89 mA h g^{-1} after 100 cycles.[57] Besides that, the G@hollow carbon electrode without FeS_2 can exhibit good cycling performance, indicating its stable carbon framework during cycles. But it delivered a relatively low capacity of 188 mA h g^{-1} after 100 cycles at 300 mA g^{-1} (Figure S15). Obviously, the G@Y-S FeS_2@C electrode delivered the best cycling stability and highest capacity among these samples. As shown in Figure 4b, it can retain a high charge capacity of 308 mA h g^{-1} after 100 cycles. Even after 1000 cycles, the capacity still remains relatively high at 270 mA h g^{-1}. The CE of this electrode quickly increased up to 95% at 10th cycle and was kept around 99-100% in the following cycles, higher than the CE values of G@FeS_2@C, G@FeS_2, and FeS_2 anodes (Figure S13). At a current density of 1 A g^{-1}, the cyclability of the G@Y-S FeS_2@C anode also outperformed the other three anodes. In Figure 4c, this anode can be seen to sustain a capacity of 162 mA h g^{-1} after 1000 cycles with an average capacity loss of 0.05% per cycle. On the other hand, the G@FeS_2@C, G@FeS_2, and FeS_2 electrodes presented rapid capacity fading and only sustained low capacities of 43, 23, and 13 mA h g^{-1} after 400 cycles, respectively. As compared with the reported PIB anode materials in Table S1, the G@Y-S FeS_2@C composite with rational microstructure design

displayed enhanced electrochemical performance in terms of specific capacity and cycling stability.

The rate performance of the G@Y-S FeS_2@C electrode was evaluated under various rates from 0.15 to 15 A g^{-1}. **Figure 5**a shows the discharge/charge profiles of the G@Y-S FeS_2@C electrode, which display similar shape and show high specific capacities even at high rates. Figure 5b compares the rate performance of G@Y-S FeS_2@C and Y-S FeS_2@C composite, demonstrating the positive effect of graphene matrix on the performance of yolk-shell structure. At a low current density of 0.15 A g^{-1}, G@Y-S FeS_2@C anode can deliver a high initial charge capacity of 521 mA h g^{-1}. When cycled at high rates of 1, 2, 4, 6, 10 A g^{-1}, the charge capacities were sustained at high values of 360, 315, 266, 240, 203 mA h g^{-1}, respectively. Even at a large current density of 15 A g^{-1}, the specific capacity still remained at 166 mA h g^{-1}. Compared with the reported anode materials for PIBs (Figure 5c), this G@Y-S FeS_2@C composite displayed remarkable advantage at rate capabilities. When the current density was restored back to 0.15 A g^{-1}, stable capacities around 400 mA h g^{-1} can be obtained. However, the rate performance of Y-S FeS_2@C anode was inferior, only showing capacities of 290, 244, 204, 175, 144, 117 mA h g^{-1} under 1, 2, 4, 6, 10, 15 A g^{-1}, respectively. The discharge/charge profiles at various rates were shown in Figure S16. The poor rate performance of Y-S FeS_2@C could be ascribed to the poor conductivity of the amorphous carbon coating, as well as the point-to-point contact interface between FeS_2 (yolk) and carbon (shell), which retards the fast transport of both electrons and potassium ions during cycles.[58]

The effect of the graphene matrix on the electrochemical reaction kinetics of yolk-shell structure was investigated through galvanostatic intermittent titration technique (GITT) and electrochemical impedance spectroscopy (EIS) measurements. Figure S17 shows the GITT curves and the overpotential (difference between the working voltage and equilibrium voltage) under various potassium ion insertion/extraction stages. It can be seen that G@Y-S FeS_2@C exhibited smaller overpotentials than Y-S FeS_2@C, indicating its better reaction kinetics. The

K-ion diffusion coefficient (D_k) can be calculated through the simplified Fick's second law based on the GITT curves.[56, 59, 60] As shown in Figure S17, the average D_k of G@Y-S FeS_2@C at discharge and charge process were 2.0 and 2.6 times higher respectively than the equivalent values of Y-S FeS_2@C. It suggests that the graphene matrix can facilitate the K-ion diffusion in yolk-shell structure. Figure S18 shows the EIS profiles of these two electrodes. It is obvious that the G@Y-S FeS_2@C electrode exhibited a small semicircle diameter in the high-medium frequency region, indicating its low charge transfer impedance during cycles.[61-63] Based on the GITT and EIS results, it can be concluded that the graphene matrix can effectively enhance electron and potassium ion transportation of yolk-shell structure, thus resulting in the superior rate capability of G@Y-S FeS_2@C composite.

Figure S19 discloses the rate capabilities of G@FeS_2@C, G@FeS_2, and pure FeS_2 electrodes. The capacities of G@FeS_2@C electrode remained at 200, 160, and 125 mA h g^{-1} at 6, 10, and 15 A g^{-1}, respectively. However, capacity fading was found when returning to 0.15 A g^{-1}, consistent with the unstable capacity retention in Figure 4. Pure FeS_2 and G@FeS_2 electrodes only presented poor rate capabilities of 50 and 30 mA h g^{-1} at 15 A g^{-1}, and showed rapid capacity decay at 0.15 A g^{-1}. We also tested the long-term cycling stability of G@Y-S FeS_2@C electrode at high current densities. Impressively, this electrode can exhibit ultra-long cycling retention up to 1500 cycles, and retained capacities of 122 and 100 mA h g^{-1} at 2 and 5 A g^{-1}, respectively. The average capacity fading was only 0.043% per cycle. Both the capacity and cycling retention of Y-S FeS_2@C were inferior to the G@Y-S FeS_2@C electrode. It showed large capacity loss of 0.054-0.057% during cycles, and maintained low capacities of 52 and 30 mA h g^{-1} after 1500 cycles at 2 and 5 A g^{-1}. Moreover, both G@Y-S FeS_2@C and Y-S FeS_2@C electrodes exhibited better cycling retention than the G@FeS_2@C without interior void space, which suffered from fast capacity fading within the initial 200 cycles at high rates, and only had low capacities of 18 and 11 mA h g^{-1} at 2 and 5 A g^{-1} after 1500 cycles (Figure S20).

To further explain the origin of high-rate capabilities in the G@Y-S FeS_2@C electrode, the redox pseudocapacitive contribution of this electrode was studied by analyzing its reaction kinetics through CV curves at various scan rates (v) (Figure S21).[64-66] The current response (i) at a fixed potential (V) can be separated into capacitive effect (k_1v) and diffusion-controlled reaction ($k_2v^{1/2}$), according to the following equation: $i(V) = k_1v + k_2v^{1/2}$. By calculating both the k_1 and k_2 constants, we can distinguish the portion of the current from surface capacitance and diffusion-controlled capacity. At a scan sweep rate of 0.8 mV s^{-1}, the typical CV profile for the capacitive current (blue section) in comparison with total current was shown in Figure 5e, in which a dominating capacitive contribution of 72% was quantified. The ratio of capacitive contribution gradually enlarged as the scan rate increased. Seen from Figure 5h, the contributions from capacitive behavior were 61%, 72%, 75%, 77%, and 82% at scan rates of 0.4, 0.8, 1.0, 1.5, and 2.0 mV s^{-1}, respectively. These results demonstrated that the high rate capabilities of G@Y-S FeS_2@C were mainly derived from capacitance-dominated reactions. This is unsurprising since the large surface area, abundant porous structure, and small size of FeS_2 particles in G@Y-S FeS_2@C composite could be beneficial for the pseudocapacitive behavior.[67-69] Moreover, DFT calculations were performed to depict the paths and energy barriers for K^+ diffusion in $KFeS_2$ (Figure 5g), which influenced the rate performance.[70] Several paths directly connecting two adjacent K atoms were considered, including horizontal and perpendicular to the Fe-S chains. The minimum energy path was calculated to be perpendicular to the Fe-S chains with a transition point at the middle. The diffusion barriers turn out to be 0.63 eV for $KFeS_2$, which is comparable to the values of 0.34 eV for $Na_3(FeS_2)_2$ and 0.13 eV for Li_2FeS_2 (Figure S22). Thus, FeS_2 as a promising anode material for PIBs can exhibit high capacity and good rate performance.

Furthermore, the G@Y-S FeS_2@C composite delivered outstanding sodium storage performance as well (Figure S23). As an anode material for SIBs, it showed a high initial charge capacity of 644 mA h g^{-1} at 300 mA g^{-1}, and sustained a good capacity retention of

88% after 100 cycles. Even at high rates of 10 and 15 A g^{-1}, the specific capacities still remained at high values of 468 and 451 mA h g^{-1}, respectively. The rate capabilities were much higher than the as-reported yolk-shell FeS_x@C anode (403 mA h g^{-1} at 5 A g^{-1}), due to the existence of a conductive graphene matrix and the small size of FeS_2.[51, 71] To the best of our knowledge, our G@Y-S FeS_2@C anode displays the best rate capabilities among the FeS_2-based anodes for SIBs, as confirmed in Table S2. Further extending the cycling test at 2 A g^{-1} after various rates, this electrode still presented remarkable cycling stability and maintained a capacity of 336 mA h g^{-1} even after 2000 cycles. Both of the sodium and potassium storage properties of G@Y-S FeS_2@C composite are superior in terms of rate capabilities and cycling stability to those of the as-reported metal sulfide anodes in the literature (Table S1-2), suggesting the effectiveness of rational microstructure design in enhancing electrochemical performance.

The structural evolutions of the electrodes after several potassiation/depotassiation cycles were further examined through post-mortem SEM observations in Figure S24. The G@FeS_2@C electrode without interior void space suffered from severe agglomeration of active materials after cycles, and was covered with thick SEI films. This is probably due to the huge volume variation of FeS_2 during cycles, leading to the cracking of carbon shells, particle aggregation, and continuous growth of SEI film. The Y-S FeS_2@C electrode can maintain the nanorod morphology without the breaking of the carbon layer. The SEM images in Figure S24 further confirmed the structural stability of G@Y-S FeS_2@C composite, from which the yolk-shell nanorods were seen to be well-maintained and still anchored on the graphene matrix after 50 cycles. In the TEM observations (Figure S25), we can also observe the yolk-shell structure with active materials still confined within carbon shells after cycles. Moreover, the EDS pattern showed that after 50 cycles, the S/Fe ratios in G@Y-S FeS_2@C, Y-S FeS_2@C, and G@FeS_2@C electrodes were 1.82, 1.65, and 1.57, respectively. These results illustrated that the stable carbon coating shell and graphene matrix in G@Y-S FeS_2@C

composite can efficiently hamper the dissolution of the sulfur component during cycles.[48, 72, 73] On the basis of the above observations, the superior electrochemical performance of G@Y-S FeS_2@C electrode can be mainly attributed to its unique architectural properties. In particular, the yolk-shell structure can supply sufficient empty space for the volume expansion of FeS_2 during potassiation/depotassiation processes. The rigid carbon coating shell can effectively hamper sulfur dissolution, facilitate the formation of a stable SEI layer, and, more importantly, prevent the aggregation of FeS_2 during cycles. These factors result in high capacity, good coulumbic efficiency, and excellent cycling stability. Moreover, the highly conductive graphene matrix and carbon coating are beneficial for fast electron and ion transportation, and the small size of FeS_2 can shorten the K^+ diffusion path, thus leading to excellent rate capability.

3. Conclusion

In summary, we presented a superior PIB anode material by rationally *in-situ* engineering a yolk-shell FeS_2@C composite on a graphene matrix. Benefiting from the yolk-shell structure to provide interior void space and protective carbon coating, and the graphene matrix to enable fast transport of electrons and ions, the G@Y-S FeS_2@C anode exhibited high specific capacity and excellent rate performance (166 mA h g^{-1} at 15 A g^{-1}). Remarkably, it also delivered long-term cycling stability up to 1500 cycles at high rates of 2 and 5 A g^{-1}. Investigation into the potassium storage mechanism of FeS_2 anode disclosed its reversible intercalation/deintercalation and conversion reactions upon cycling. In addition, the microstructure design strategy in this study could also be applied to other anodes with large volume variation for superior alkali metal ion (Li^+, Na^+, and K^+) storage performance.

4. Experimental Section

Synthesis of G@Fe_3O_4@C composite: The graphene oxide (GO) was fabricated through a modified Hummer's method. Then, 60 mg GO and 3.24 g $FeCl_3.6H_2O$ were dispersed in 150

mL de-ionized water and stirred at 75 °C for 24 h. The obtained GO@FeOOH (150 mg) was sonicated in 18.6 mL H_2O for 1 h, followed with the addition of 0.048 mL $NH_3.H_2O$ and 0.6 mL 0.01 M cetyltrimethylammonium bromide (CTAB) aqueous solution. After stirred for 0.5 h, 24 mg resorcinol and 0.0336 mL formaldehyde solution were added into the above solution and kept under stirring for 16 h at room temperature. The product was filtered and washed with water, dried at 80 °C overnight, and carbonized at 550 °C for 2 h under Ar atmosphere, to obtain G@Fe_3O_4@C composite.

Synthesis of G@Y-S Fe_3O_4@C composite: In a typical synthesis, as-obtained G@Fe_3O_4@C (80 mg) sample was dispersed in 40 mL 1 M HCl mixed solvent (10 mL ethanol and 30 mL H_2O) with stable stirring for various hours. G@Y-S Fe_3O_4@C composite was obtained after 8 h etching time, filtered and washed with ethanol and water, and dried at 70 °C for 12 h. By further increasing the etching time up to 48 h, Fe_3O_4 was completely etched away to obtain G@hollow carbon composite. Y-S Fe_3O_4@C composite was synthesized through similar procedure with G@Y-S Fe_3O_4@C composite without the addition of GO.

Synthesis of G@Y-S FeS_2@C composite: In a typical experiment, 40 mg G@Y-S Fe_3O_4@C and 60 mg sulfur were mixed and sealed in a quartz tube under vacuum, and annealed at 500 °C for 3h with a heating rate of 5 °C min^{-1}. The resulting power was further heated at 350 °C for 1h to evaporate the excess sulfur. As-synthesized produce was denoted as G@Y-S FeS_2@C. The pure FeS_2, G@FeS_2, G@FeS_2@C, and Y-S FeS_2@C composites were also prepared under the same process with pure Fe_3O_4, GO@FeOOH, G@Fe_3O_4@C, and Y-S Fe_3O_4@C composites as precursors, respectively.

Materials Characterization: The microscopic and structure characterizations of the samples were carried out through transmission electron microscope (TEM, FEI Tecani G2 F20), scanning electron microscopy (SEM, SU-8010), and X-ray diffraction (XRD, Shimadzu Miniflex600). The specific surface area and pore structure of the composite were measured via Brunauer–Emmett–Teller surface area analyzer (BET, Quantachrome Autosorb-iQ2-XR).

Thermogravimetry analyses (TGA, NETZSCH STA449C) were performed from 30 to 800 °C at a heating rate of 10 K min^{-1} in air.

Computational Methods: The total energy calculations are performed in the framework of density functional theory using projector augmented wave method as implemented in Vienna Ab-initio Simulation Package. The generalized gradient approximation of Perdew, Burke and Ernzerhof is employed for the exchange-correlation potential. The cut-off energy for plane-wave basis sets is set to 300 eV. The Brillouin zone integrations are performed using a 4×2×8 k-mesh for $KFeS_2$ and for 4×2×2 for $K_3(FeS_2)_2$. An energy criterion of 10^{-6} eV is used in the iterative solution of the Kohn-Sham equation. The structures are relaxed until the residual forces on the atoms have declined to less than 0.01 eV/A. Diffusion barriers are calculated by the climbing image nudged elastic band method with 5 images between the initial and final configurations.

Electrochemical measurements: The electrochemical performance of the composites was conducted via CR2025 coin cells. The working electrodes were composed of active materials, ketjen black carbon, and carboxymethyl cellulose (80:10:10 in weight), which were mixed with de-ionized water, pasted on Ni foam, and dried at 80 °C under vacuum before use. The cells were assembled in an argon-filled glove box and tested in a battery tester (LAND 2001A system). For PIBs, the electrolyte was 1 M KPF_6 in ethylene carbonate (EC): propylene carbonate (PC) (1:1 in volume). For SIBs, 1 M $NaClO_4$ in EC: diethyl carbonate (DEC) (1:1 in volume) with 10 wt% fluoroethylene (FEC) was used as the electrolyte. Potassium and sodium foils were the counter electrodes for PIBs and SIBs, respectively. A glass fiber membrane (Whatman, GF/D) was used as the separator. Cells were discharged and charged over a voltage range of 0.05 V and 2.8 V at various current densities from 0.15 to 15 A g^{-1}. Cyclic voltammetry (CV) was tested on a CHI660C electrochemical workstation under various scan rates.

Supporting Information

Supporting Information is available from the Wiley Online Library or from the author.

Acknowledgements

This work was supported by National Natural Science Foundation of China (Grant 21701174), the Youth Innovation Promotion Association CAS, NSF for Distinguished Young Scholars of Fujian Province (Grant 2017J07004), the Science and Technology Planning Project of Fujian Province (Grant 2017J05096), the Singapore Ministry of Education Tier 2 Grant (MOE2017-T2-1-009) and Tier 1 Grant (RG3/17(S)), the National Research Foundation, Prime Minister's Office, Singapore under its Campus for Research Excellence and Technological Enterprise (CREATE) programme.

Received: ((will be filled in by the editorial staff))
Revised: ((will be filled in by the editorial staff))
Published online: ((will be filled in by the editorial staff))

References

[1] M. Armand, J. M. Tarascon, *Nature*, **2008**, *451*, 652.

[2] B. Dunn, H. Kamath, J. M. Tarascon, *Science*, **2011**, *334*, 928.

[3] D. Larcher, J. M. Tarascon, *Nat. Chem.*, **2015**, *7*, 19.

[4] S. Chu, Y. Cui, N. Liu, *Nat. Mater.*, **2017**, *16*, 16.

[5] C. P. Grey, J. M. Tarascon, *Nat. Mater.*, **2017**, *16*, 45-56.

[6] N. Yabuuchi, K. Kubota, M. Dahbi, S. Komaba, *Chem. Rev.*, **2014**, *114*, 11636.

[7] J. Y. Hwang, S. T. Myung, Y. K. Sun, *Chem. Soc. Rev.*, **2017**, *46*, 3529.

[8] J. Q. Deng, W. B. Luo, S. L. Chou, H. K. Liu, S. X. Dou, *Adv. Energy Mater.*, **2018**, *8*, 1701428.

[9] H. Kim, J. C. Kim, M. Bianchini, D. H. Seo, J. Rodriguez-Garcia, G. Ceder, *Adv. Energy Mater.*, **2018**, *8*, 1702384.

[10] J. C. Pramudita, D. Sehrawat, D. Goonetilleke, N. Sharma, *Adv. Energy Mater.*, **2017**, *7*, 1602911.

[11] X. X. Zou, P. X. Xiong, J. Zhao, J. M. Hu, Z. T. Liu, Y. H. Xu, *Phys. Chem. Chem. Phys.*, **2017**, *19*, 26495.

[12] I. Sultana, M. M. Rahman, Y. Chen. A. M. Glushenkov, *Adv. Funct. Mater.*, **2018**, *28*, 1703857.

[13] Z. L. Jian, W. Luo. X. L. Ji, *J. Am. Chem. Soc.*, **2015**, *137*, 11566.

[14] J. Zhao, X. X. Zou, Y. J. Zhu, Y. H. Xu. C. S. Wang, *Adv. Funct. Mater.*, **2016**, *26*, 8103.

[15] W. Wang, J. H. Zhou, Z. P. Wang, L. Y. Zhao, P. H. Li, Y. Yang, C. Yang, H. X. Huang, S. J. Guo, *Adv. Energy Mater.*, **2018**, *8*, *1701648.*

[16] X. X. Zhao, P. X. Xiong, J. F. Meng, Y. Q. Liang, J. W. Wang, Y. H. Xu, *J. Mater. Chem. A*, **2017**, *5*, 19237.

[17] X. P. Wang, K. Han, D. D. Qin, Q. Li, C. Y. Wang, C. J. Niu, L. Q. Mai, *Nanoscale*, **2017**, *9*, 18216.

[18] Z. C. Ju, S. Zhang, Z. Xing, Q. C. Zhuang, Y. H. Qiang, Y. T. Qian, *ACS Appl. Mater. Inter.*, **2016**, *8*, 20682.

[19] Y. H. Xie, Y. Chen, L. Liu, P. Tao, M. P. Fan, N. Xu, X. W. Shen, C. L. Yan, *Adv. Mater.*, **2017**, *29*, 1701648.

[20] P. X. Xiong, X. X. Zhao, Y. H. Xu, *Chemsuschem*, **2018**, *11*, 202.

[21] J. L. Yang, Z. C. Ju, Y. Jiang, Z. Xing, B. J. Xi, J. K. Feng, S. L. Xiong, *Adv. Mater.*, **2018**, *30*, 1700104.

[22] I. Sultana, T. Ramireddy, M. M. Rahman, Y. Chen, A. M. Glushenkov, *Chem. Commun.*, **2016**, *52*, 9279.

[23] I. Sultana, M. M. Rahman, T. Ramireddy, Y. Chen, A. M. Glushenkov, *J. Mater. Chem. A*, **2017**, *5*, 23506.

[24] W. C. Zhang, J. F. Mao, S. A. Li, Z. X. Chen, Z. P. Guo, *J. Am. Chem. Soc.*, **2017**, *139*, 3316.

[25] J. H. Zhou, L. Wang, M. Y. Yang, J. H. Wu, F. J. Chen, W. J. Huang, N. Han, H. L. Ye, F. P. Zhao, Y. Y. Li, Y. G. Li, *Adv. Mater.*, **2017**, *29*, 1702061.

[26] I. Sultana, M. M. Rahman, S. Mateti, V. G. Ahmadabadi, A. M. Glushenkov, Y. Chen, *Nanoscale*, **2017**, *9*, 3646.

[27] Y. Y. Lu, J. Chen, *Sci. China Chem.*, **2017**, *60*, 1533.

[28] K. Y. Xie, K. Yuan, X. Li, W. Lu, C. Shen, C. L. Liang, R. Vajtai, P. Ajayan, B. Q. Wei, *Small*, **2017**, *13*, 1701471.

[29] M. L. Mao, C. Y. Cui, M. G. Wu, M. Zhang, T. Gao, X. L. Fan, J. Chen, T. H. Wang, J. M. Ma, C. S. Wang, *Nano Energy*, **2018**, *45*, 346.

[30] Y. Zhao, L. P. Wang, M. T. Sougrati, Z. X. Feng, Y. Leconte, A. Fisher, M. Srinivasan, Z. C. Xu, *Adv. Energy Mater.*, **2017**, *7*, 1601424.

[31] J. Cui, S. Yao, J.-K. Kim, *Energy Storage Materials*, **2017**, *7*, 64.

[32] C. B. Zhu, R. E. Usiskin, Y. Yu, J. Maier, *Science*, **2017**, *358*, 1400.

[33] Z. S. Wu, G. M. Zhou, L. C. Yin, W. Ren, F. Li, H. M. Cheng, *Nano Energy*, **2012**, *1*, 107.

[34] R. Raccichini, A. Varzi, S. Passerini and B. Scrosati, *Nat. Mater.*, **2015**, *14*, 271.

[35] G. Pengbiao, Z. Shasha, T. Hao, Z. Rongmei, Z. Li, C. Shuai, X. Huaiguo, P. Huan, *Adv. Energy Mater.*, **2018**, *8*, 1703259.

[36] H. T. Sun, L. Mei, J. F. Liang, Z. P. Zhao, C. Lee, H. L. Fei, M. N. Ding, J. Lau, M. F. Li, C. Wang, X. Xu, G. L. Hao, B. Papandrea, I. Shakir, B. Dunn, Y. Huang, X. F. Duan, *Science*, **2017**, *356*, 599.

[37] V. Lakshmi, Y. Chen, A. A. Mikhaylov, A. G. Medvedev, I. Sultana, M. M. Rahman, O. Lev, P. V. Prikhodchenko, A. M. Glushenkov, *Chem. Commun.*, **2017**, *53*, 8272.

[38] H. Gao, T. F. Zhou, Y. Zheng, Q. Zhang, Y. Q. Liu, J. Chen, H. K. Liu, Z. P. Guo, *Adv. Funct. Mater.*, **2017**, *27*, 1702634.

[39] K. F. Chen, S. Y. Song, F. Liu, D. F. Xue, *Chem. Soc. Rev.*, **2015**, *44*, 6230.

[40] Z. Hu, Q. N. Liu, S. L. Chou, S. X. Dou, *Adv. Mater.*, **2017**, *29*, 1700606.

[41] Z. Y. Wang, D. Y. Luan, S. Madhavi, Y. Hu, X. W. Lou, *Energy Environ. Sci.*, **2012**, *5*, 5252.

[42] Y. Zhao, C. Wei, S. N. Sun, L. P. Wang, Z. C. J. Xu, *Adv. Sci.*, **2015**, *2*, 1500097.

[43] Z. Liu, X. Y. Yu, U. Paik, *Adv. Energy Mater.*, **2016**, *6*, 1502318.

[44] Y. Zhao, Z. X. Feng, Z. C. J. Xu, *Nanoscale*, **2015**, *7*, 9520.

[45] Y. Z. Li, K. Yan, H. W. Lee, Z. D. Lu, N. Liu, Y. Cui, *Nat. Energy*, **2016**, *1*, 15029.

[46] C. Wu, X. Tong, Y. F. Ai, D. S. Liu, P. Yu, J. Wu, Z. M. M. Wang, *Nano-Micro Lett.*, **2018**, *10*, 40.

[47] A. Kitajou, J. Yamaguchi, S. Hara, S. Okada, *J. Power Sources*, **2014**, *247*, 391.

[48] K. Y. Chen, W. X. Zhang, L. H. Xue, W. L. Chen, X. H. Xiang, M. Wan, Y. H. Huang, *ACS Appl. Mater. Inter.*, **2017**, *9*, 1536.

[49] S. S. Zhang, *J. Mater. Chem. A*, **2015**, *3*, 7689.

[50] A. Douglas, R. Carter, L. Oakes, K. Share, A. P. Cohn, C. L. Pint, *ACS Nano*, **2015**, *9*, 11156.

[51] Z. M. Liu, T. C. Lu, T. Song, X. Y. Yu, X. W. Lou, U. Paik, *Energy Environ. Sci.*, **2017**, *10*, 1576.

[52] M. Walter, T. Zund, M. V. Kovalenko, *Nanoscale*, **2015**, *7*, 9158.

[53] Z. Hu, Z. Q. Zhu, F. Y. Cheng, K. Zhang, J. B. Wang, C. C. Chen, J. Chen, *Energy Environ. Sci.*, **2015**, *8*, 1309.

[54] G. Kresse, D. Joubert, *Phys. Rev. B*, **1999**, *59*, 1758.

[55] J. P. Perdew, K. Burke, M. Ernzerhof, *Phys. Rev. Lett.*, **1996**, *77*, 3865.

[56] Y. Zhao, L. P. Wang, S. B. Xi, Y. H. Du, Q. Q. Yao, L. H. Guan, Z. C. J. Xu, *J. Mater. Chem. A*, **2017**, *5*, 25609.

[57] Y. Zhao, B. Guo, Q. Yao, J. Li, J. Zhang, K. Hou, L. Guan, *Nanoscale*, **2018**, *10*, 7999.

[58] B. Wang, X. L. Li, X. F. Zhang, B. Luo, Y. B. Zhang, L. J. Zhi, *Adv. Mater.*, **2013**, *25*, 3560.

[59] Y. H. Xu, Y. J. Zhu, Y. H. Liu, C. S. Wang, *Adv. Energy Mater.*, **2013**, *3*, 128.

[60] K. M. Shaju, G. V. S. Rao, B. V. R. Chowdari, *Electrochim Acta*, **2003**, *48*, 2691.

[61] J. X. Li, M. Z. Zou, Y. Zhao, Y. B. Lin, H. Lai, L. H. Guan, Z. G. Huang, *Electrochim Acta*, **2013**, *111*, 165.

[62] P. Nie, X. Y. Liu, R. R. Fu, Y. T. Wu, J. M. Jiang, H. Dou, X. G. Zhang, *ACS Energy Lett.*, **2017**, *2*, 1279.

[63] Y. Y. Chen, X. D. Hu, B. Evanko, X. H. Sun, X. Li, T. Y. Hou, S. Cai, C. M. Zheng, W. B. Hu, G. D. Stucky, *Nano Energy*, **2018**, *46*, 117.

[64] S. Li, J. X. Qiu, C. Lai, M. Ling, H. J. Zhao, S. Q. Zhang, *Nano Energy*, **2015**, *12*, 224.

[65] C. J. Chen, Y. W. Wen, X. L. Hu, X. L. Ji, M. Y. Yan, L. Q. Mai, P. Hu, B. Shan, Y. H. Huang, *Nat. Commun.*, **2015**, *6*, 6929.

[66] Y. Liu, X.-Y. Yu, Y. Fang, X. Zhu, J. Bao, X. Zhou, X. W. D. Lou, *Joule*, **2018**, *2*, 725.

[67] D. L. Chao, C. R. Zhu, P. H. Yang, X. H. Xia, J. L. Liu, J. Wang, X. F. Fan, S. V. Savilov, J. Y. Lin, H. J. Fan, Z. X. Shen, *Nat. Commun.*, **2016**, *7*, 12122.

[68] G. P. Wang, L. Zhang, J. J. Zhang, *Chem. Soc. Rev.*, **2012**, *41*, 797.

[69] M. J. Zhi, C. C. Xiang, J. T. Li, M. Li, N. Q. Wu, *Nanoscale*, **2013**, *5*, 72.

[70] G. Henkelman, B. P. Uberuaga, H. Jonsson, *J. Chem. Phys.*, **2000**, *113*, 9901.

[71] Y. X. Wang, J. P. Yang, S. L. Chou, H. K. Liu, W. X. Zhang, D. Y. Zhao, S. X. Dou, *Nat. Commun.*, **2015**, *6*, 8689.

[72] A. Manthiram, Y. Z. Fu, S. H. Chung, C. X. Zu, Y. S. Su, *Chem. Rev.*, **2014**, 114, 11751.

[73] J. Li, J. Li, D. Yan, S. Hou, X. Xu, T. Lu, Y. Yao, W. Mai, L. Pan, *J. Mater. Chem. A*, **2018**, *6*, 6595.

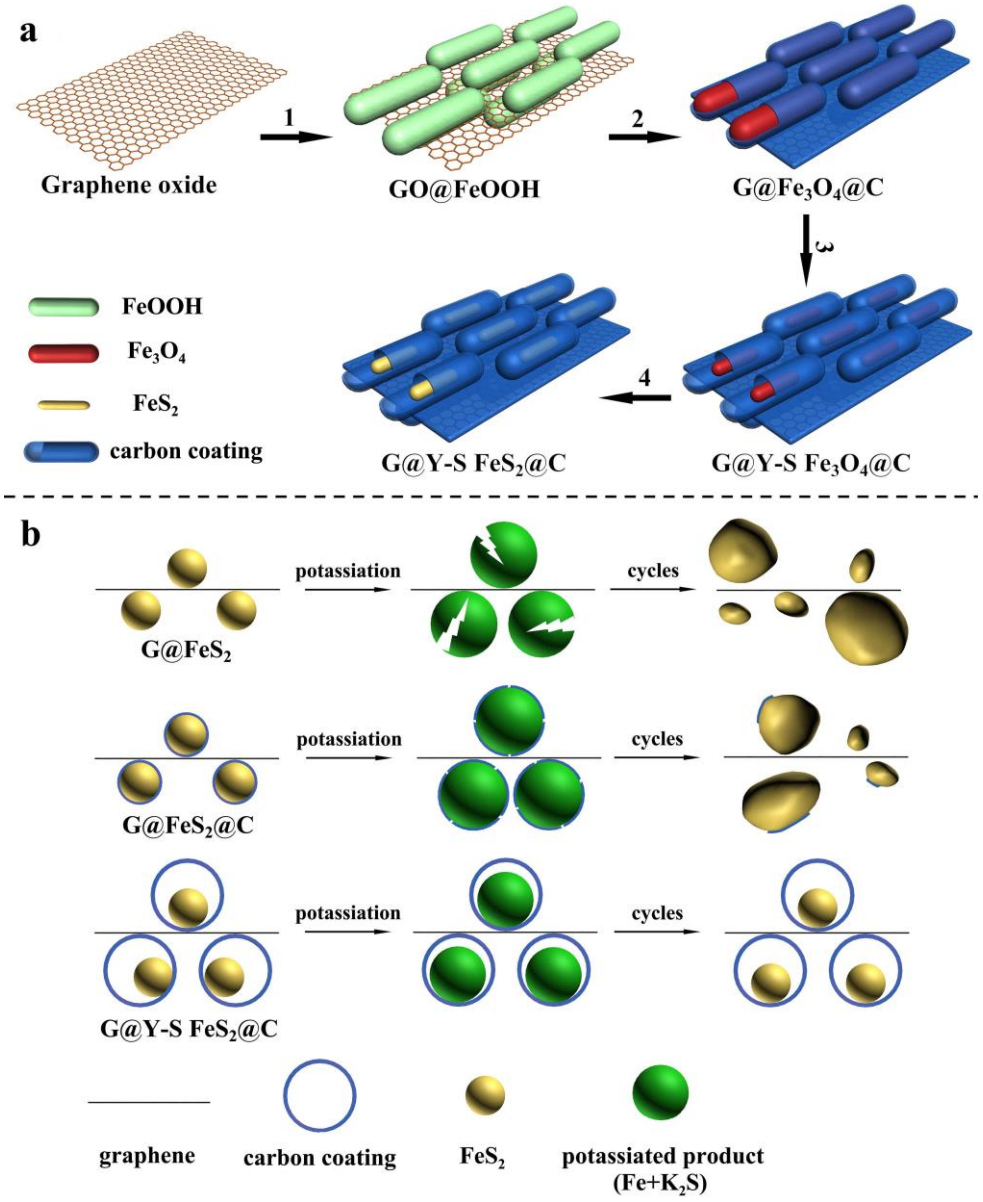

Figure 1. (a) Schematic illustration for the synthesis of G@Y-S FeS_2@C composite: 1) Formation of FeOOH nanorods on graphene oxide; 2) Coating of RF resin layer with subsequent carbonization process; 3) Etching with HCl solution to in-situ generate yolk-shell Fe_3O_4@C on graphene matrix; 4) Sulfuration treatment to synthesize G@Y-S FeS_2@C composite. (b) Schematic illustrations for the potassiation process of various graphene-FeS_2 based anodes including G@FeS_2, G@FeS_2@C, and G@Y-S FeS_2@C composites.

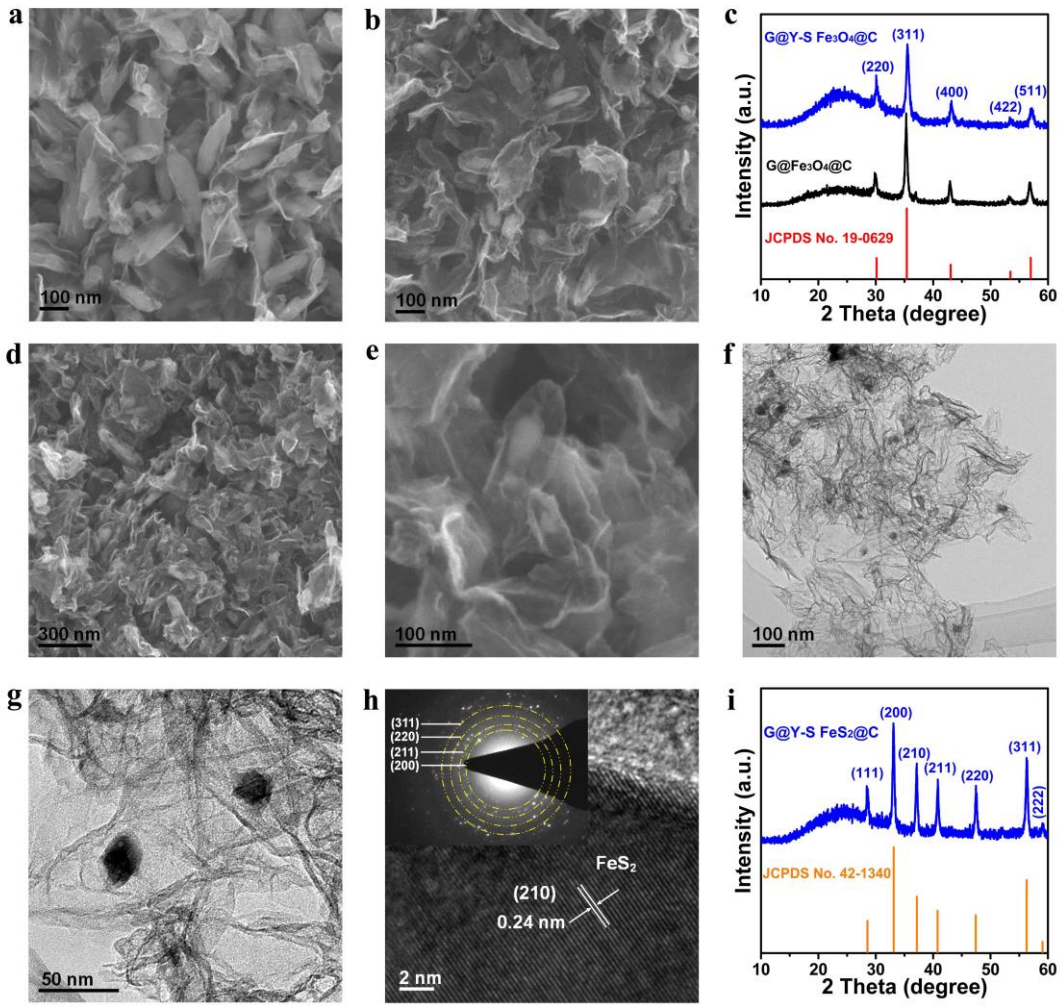

Figure 2. Morphology and structure of as-synthesized composites. SEM images of (a) G@Fe_3O_4@C, (b) G@Y-S Fe_3O_4@C, and their corresponding XRD patterns (c), showing the size reduction of Fe_3O_4 and the generation of yolk-shell structure on graphene matrix through etching process. (d-e) SEM, and (f-g) TEM images of G@Y-S FeS_2@C composite, disclosing the homogeneous distribution of yolk-shell FeS_2@C structure on graphene matrix. (h) HRTEM image (inset: corresponding SAED pattern), and (i) XRD pattern of G@Y-S FeS_2@C composite, demonstrating the formation of pyrite FeS_2 in this composite after sulfuration treatment.

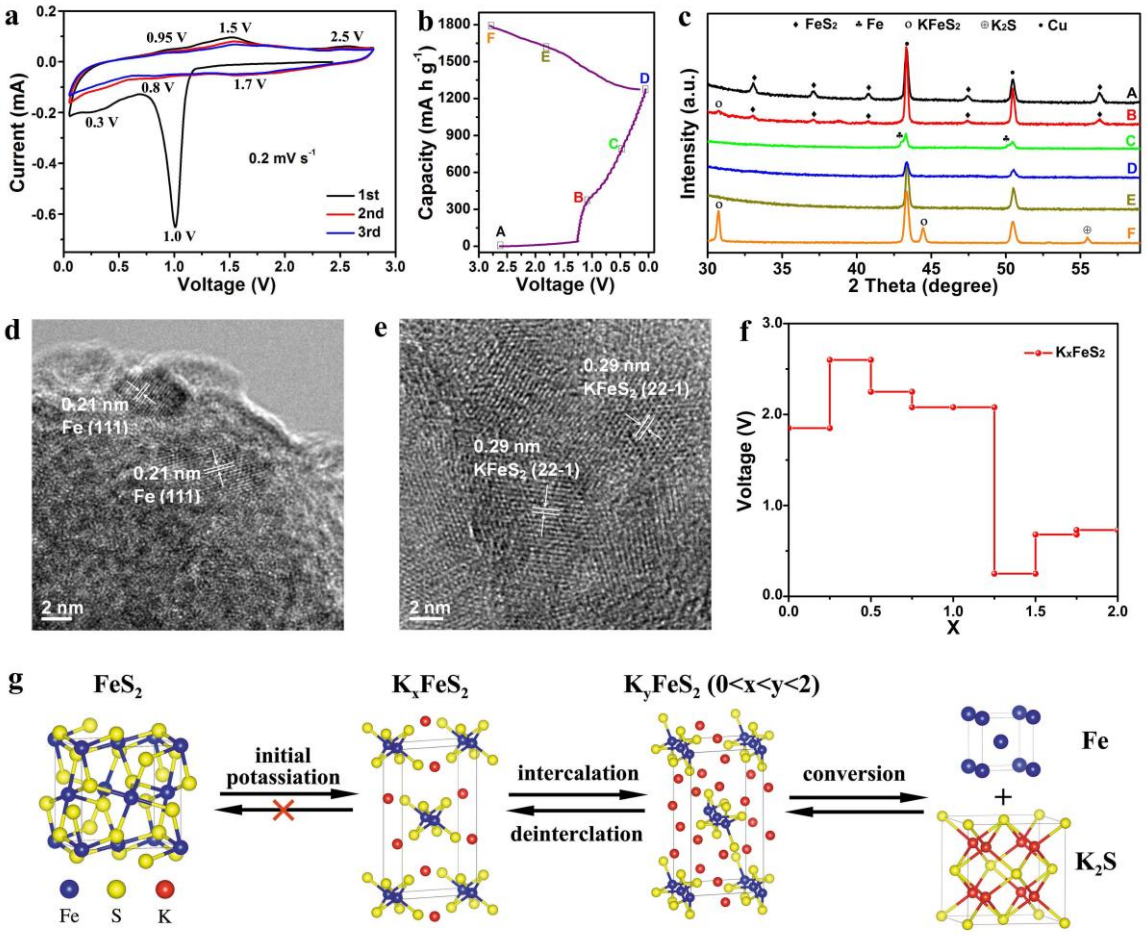

Figure 3. Potassium storage mechanism of FeS_2 anode. (a) Cyclic voltammetry curves of pure FeS_2 anode at a scan rate of 0.2 mV s^{-1}, (b) initial discharge-charge curves at 50 mA g^{-1}, and (c) *ex-situ* XRD patterns of FeS_2 electrode under various states. HRTEM images of G@Y-S FeS_2@C electrode after initial discharge to 0.05 V (d), and after initial charge to 2.8 V (e). (f) Theoretical voltage plateaus of K_xFeS_2 phase as a function of x. (g) Schematic illustration for the potassium storage reaction mechanism of FeS_2 anode, disclosing its reversible intercalation/deintercalation and conversion reactions during cycles. The Fe, S, and K atoms are shown in blue, yellow, and red color.

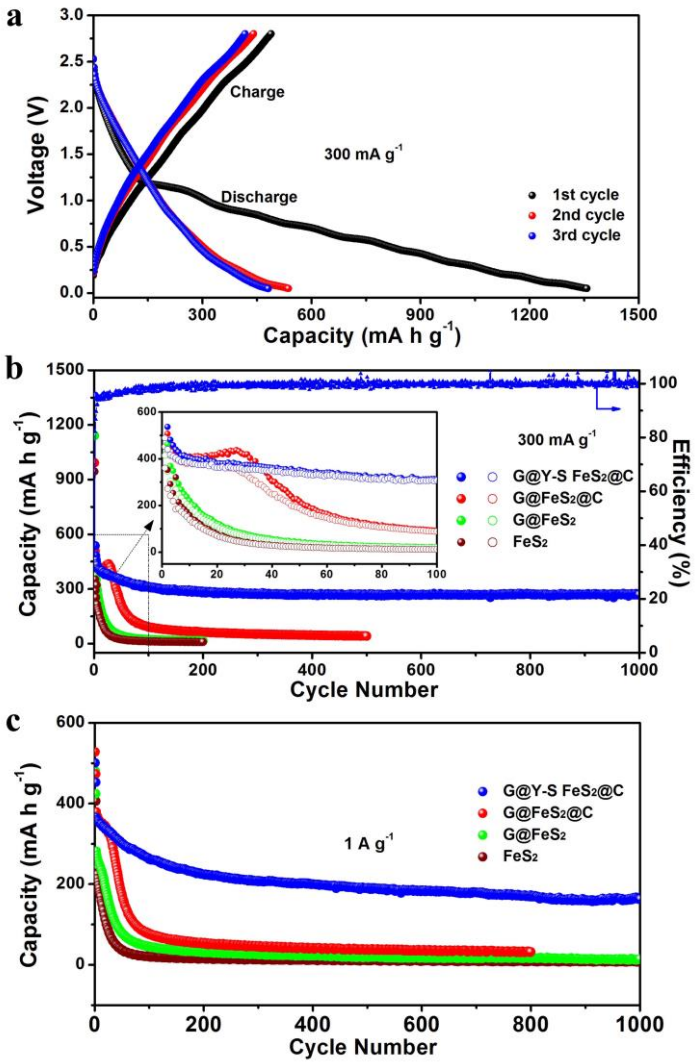

Figure 4. Cycling performance of FeS_2-based anodes for PIBs. (a) Discharge and charge profiles of G@Y-S FeS_2@C electrode for the initial three cycles at 300 mA g^{-1}. Cycling performance of G@Y-S FeS_2@C, G@FeS_2@C, G@FeS_2, and FeS_2 electrodes at current densities of (b) 0.3 A g^{-1}, and (c) 1 A g^{-1}. Inset in (b) shows the cyclability of these electrodes between 1 and 100 cycles.

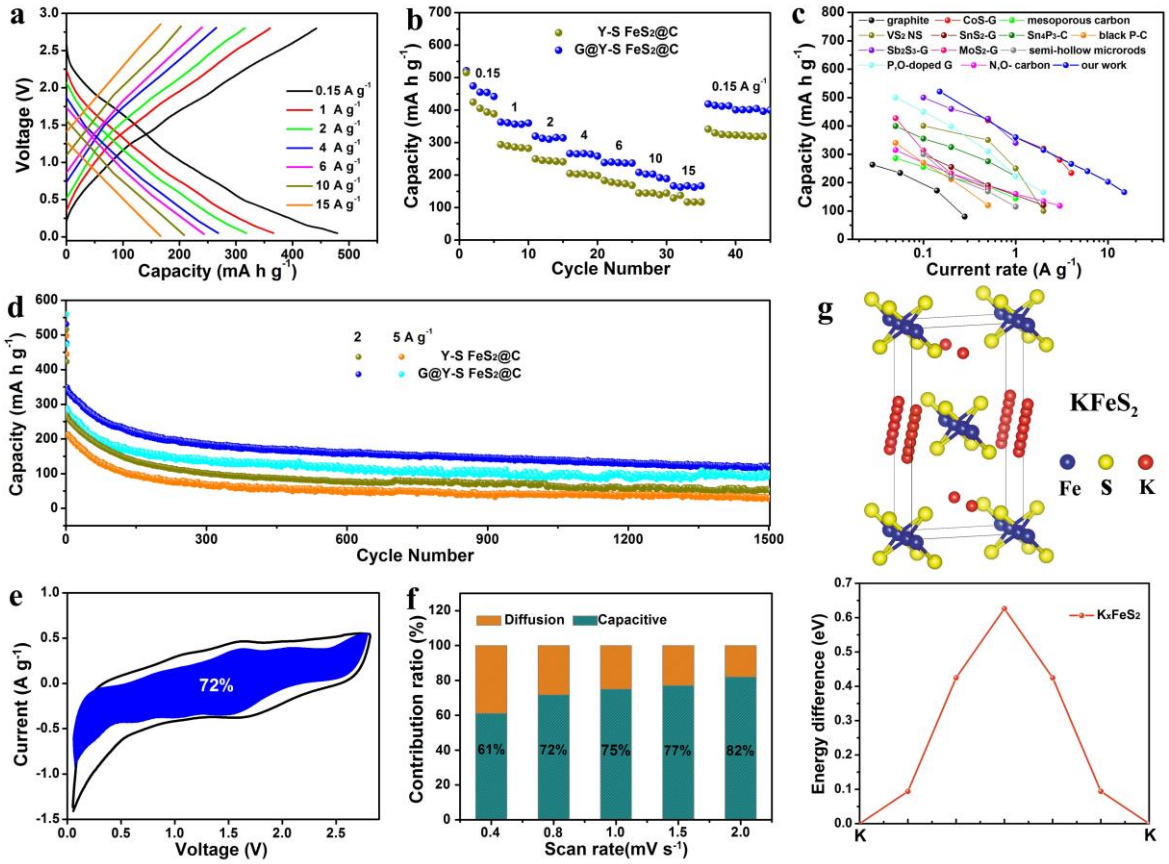

Figure 5. Rate performance of G@Y-S FeS_2@C anode for PIBs. (a) Discharge/charge profiles of G@Y-S FeS_2@C anode under various rates. (b) Rate capabilities of G@Y-S FeS_2@C and Y-S FeS_2@C electrodes from 0.15 to 15 A g^{-1}. (c) Comparison of rate capabilities between G@Y-S FeS_2@C and the as-reported anode materials for PIBs. (d) Long-term cycling stability of G@Y-S FeS_2@C and Y-S FeS_2@C electrodes at high current densities of 2 and 5 A g^{-1}. (e) CV curve with the capacitive contribution (blue section) to the total current at 0.8 mV s^{-1}, and (f) contribution ratio of the capacitive and diffusion-controlled capacities at different scan rates for G@Y-S FeS_2@C electrode. (g) Paths and energy barriers for K^+ diffusion in $KFeS_2$. The Fe, S, and K atoms are shown in blue, yellow, and red color.

***In-situ* engineering of yolk-shell FeS_2@C structure on graphene matrix** is carried out to fabricate high performance PIB anodes. Benefiting from the structural advantages with yolk-shell structure for superior structure stability and graphene matrix for fast electron/ion transportation, this anode delivers high capacity, good rate capability (203 mA h g^{-1} at 10 A g^{-1}), and remarkable long-term stability up to 1500 cycles at high rates.

Keyword: yolk-shell structure; FeS_2 anode; graphene; carbon coating; potassium-ion batteries

Yi Zhao, Jiajie Zhu, Samuel Jun Hoong Ong, Qianqian Yao, Xiuling Shi, Kun Hou, Zhichuan J. Xu, Lunhui Guan**

High-Rate and Ultralong Cycle-Life Potassium Ion Batteries Enabled by In-Situ Engineering of Yolk-Shell FeS_2@C Structure on Graphene Matrix

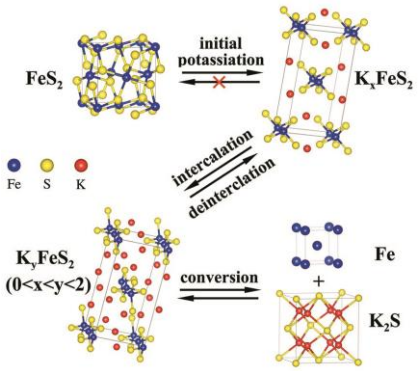

Supporting Information

High-Rate and Ultralong Cycle-Life Potassium Ion Batteries Enabled by In-Situ Engineering of Yolk-Shell FeS_2@C Structure on Graphene Matrix

Yi Zhao, Jiajie Zhu, Samuel Jun Hoong Ong, Qianqian Yao, Xiuling Shi, Kun Hou, Zhichuan J. Xu, Lunhui Guan**

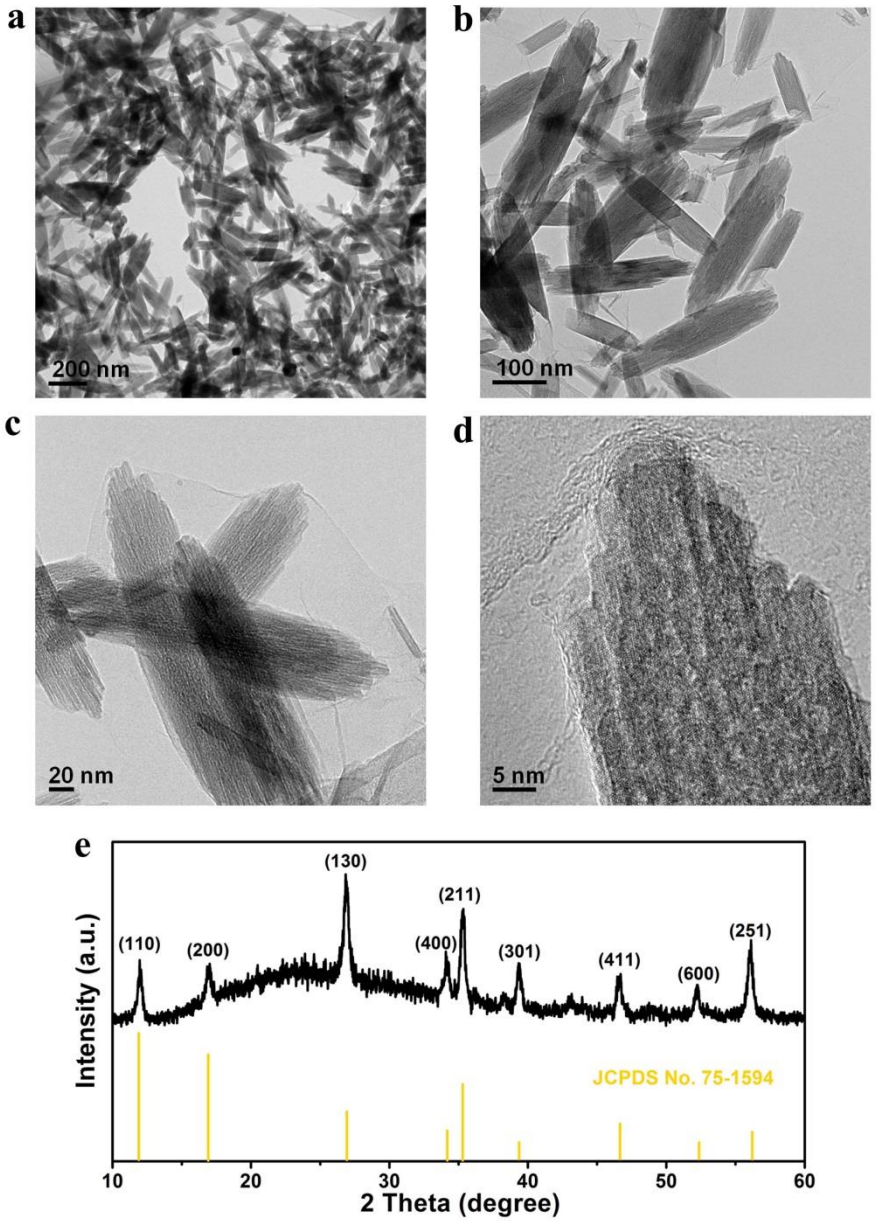

Figure S1. (a-d) TEM images, and (e) XRD pattern of GO@FeOOH composite.

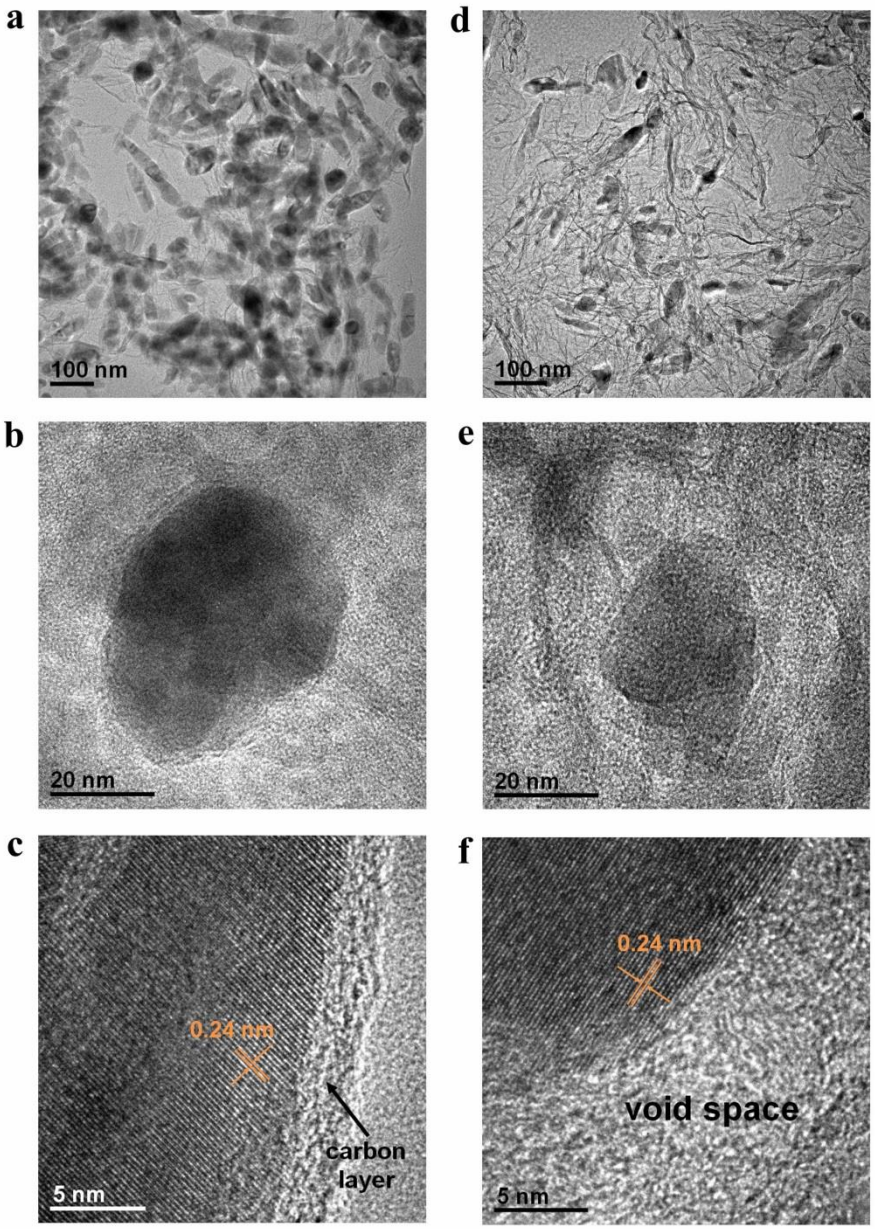

Figure S2. (a, b, d, e) TEM and (c, f) HRTEM images of (a-c) G@Fe_3O_4@C, and (d-f) G@Y-S Fe_3O_4@C composites.

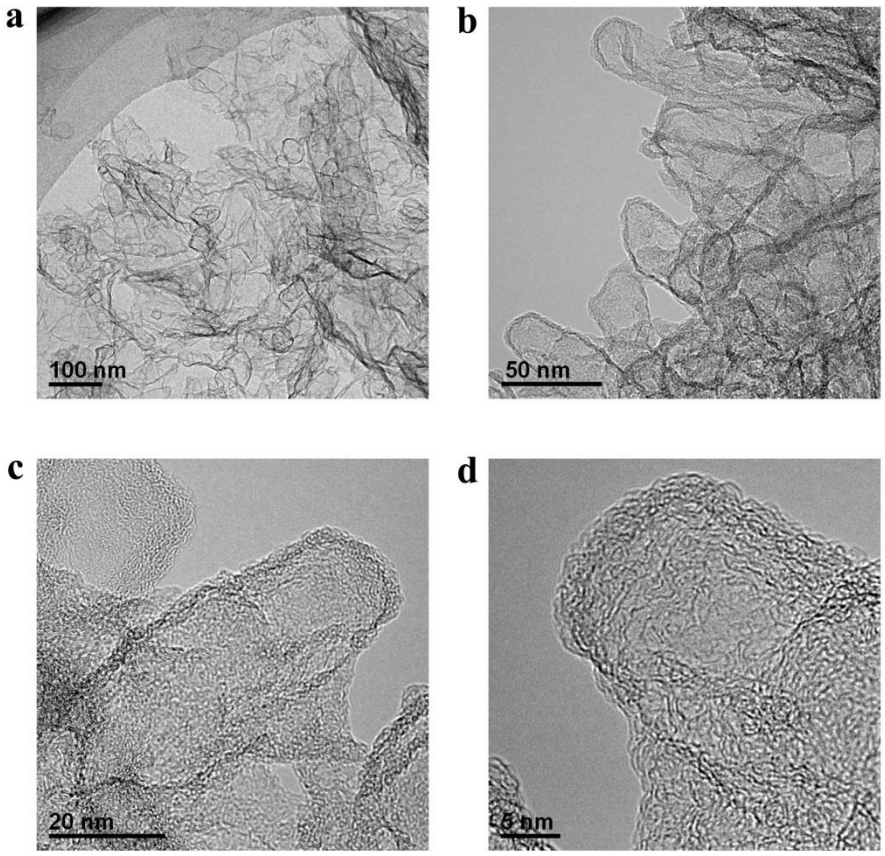

Figure S3. (a-d) TEM images of G@hollow carbon composite after etching with HCl for 48h, from which hollow carbon particles were anchored on graphene matrix.

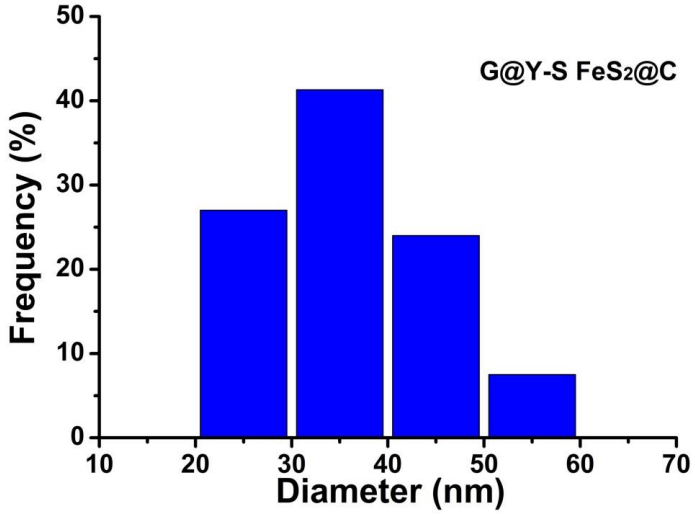

Figure S4. Diameter distribution of FeS_2 in G@Y-S FeS_2@C composite.

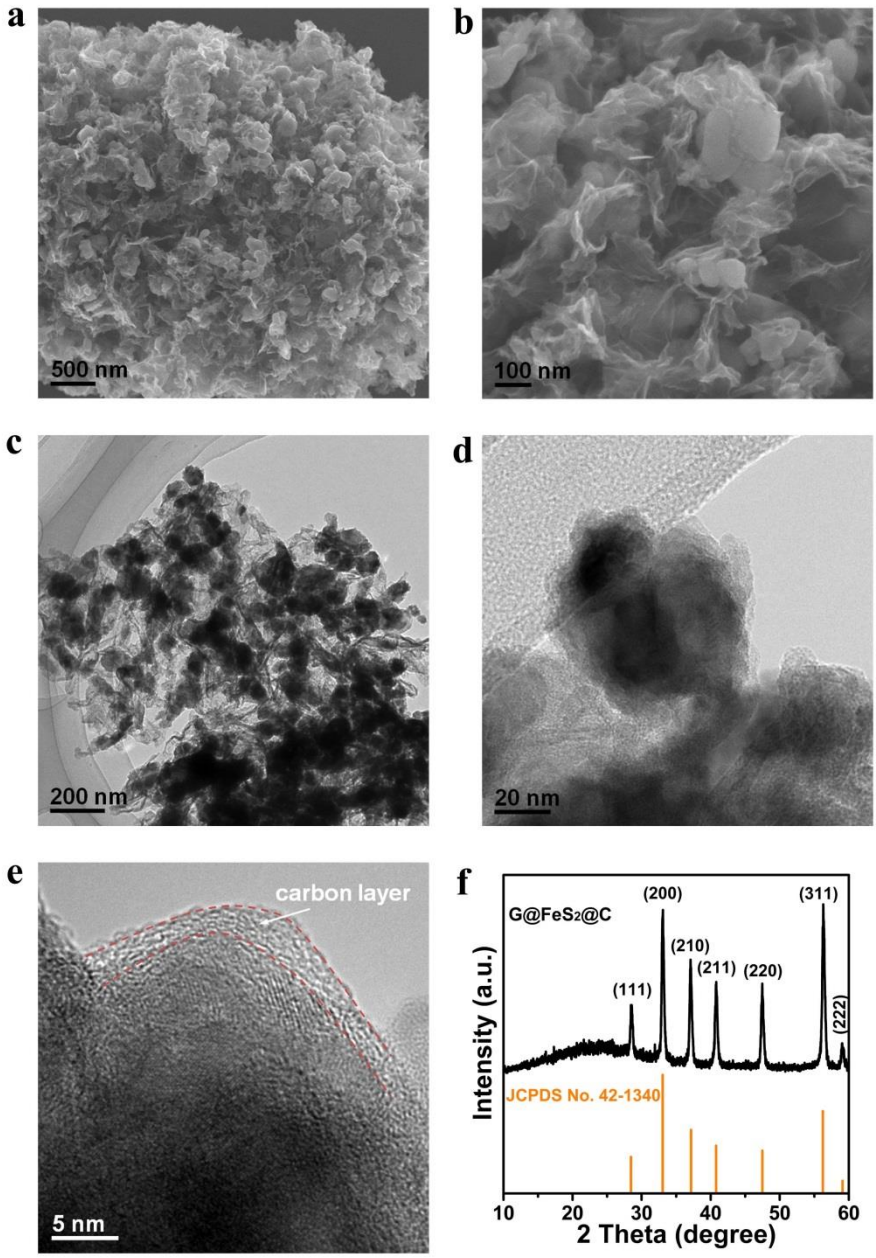

Figure S5. (a-b) SEM, (c-e) TEM images and (f) XRD pattern of G@FeS_2@C composite.

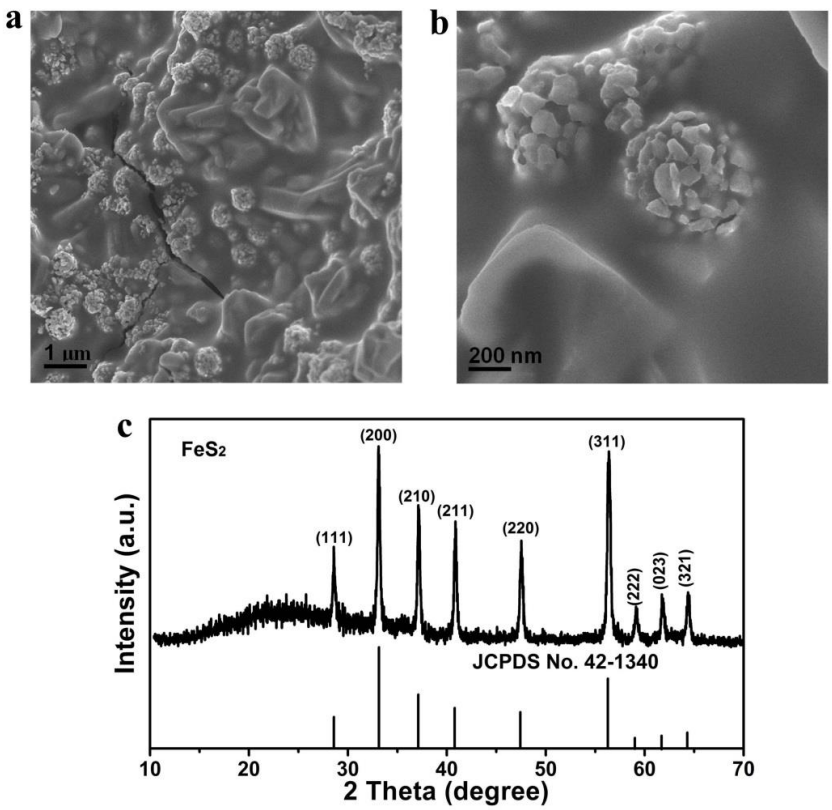

Figure S6. (a-b) SEM images and (c) XRD pattern of pure FeS_2 after sulfuration treatment of Fe_3O_4 particles.

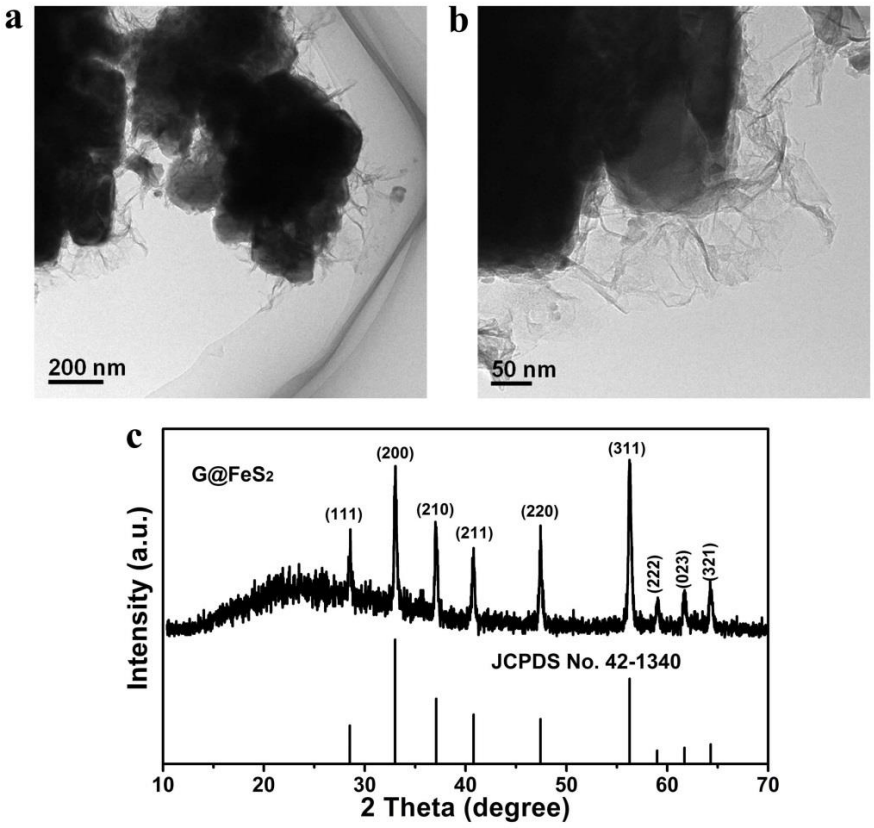

Figure S7. (a-b) TEM images and (c) XRD profile of G@FeS_2 composite after sulfuration treatment of GO@FeOOH composite.

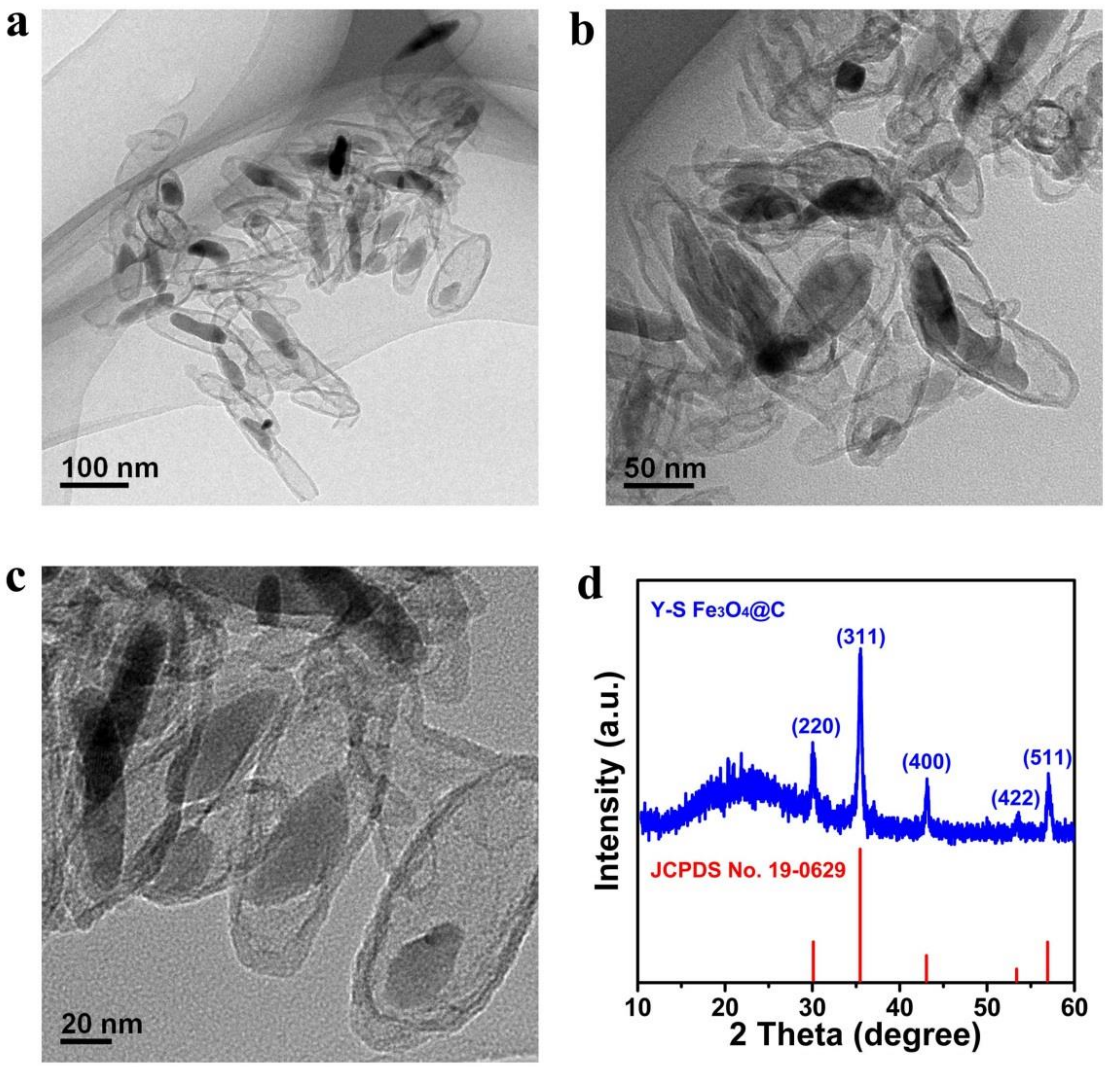

Figure S8. (a-c) TEM images and (d) XRD pattern of Y-S Fe_3O_4@C composite.

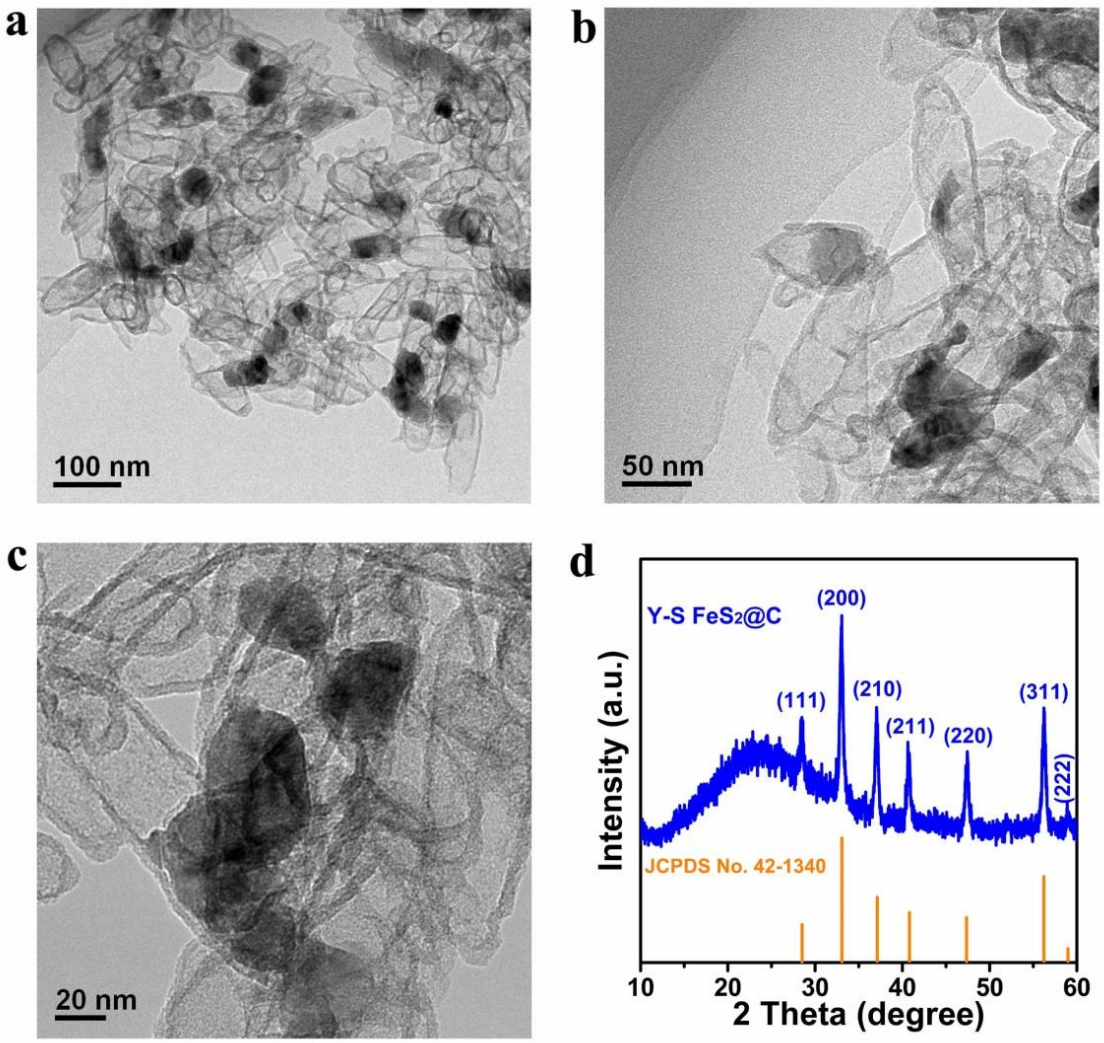

Figure S9. (a-c) TEM images and (d) XRD pattern of Y-S FeS_2@C composite.

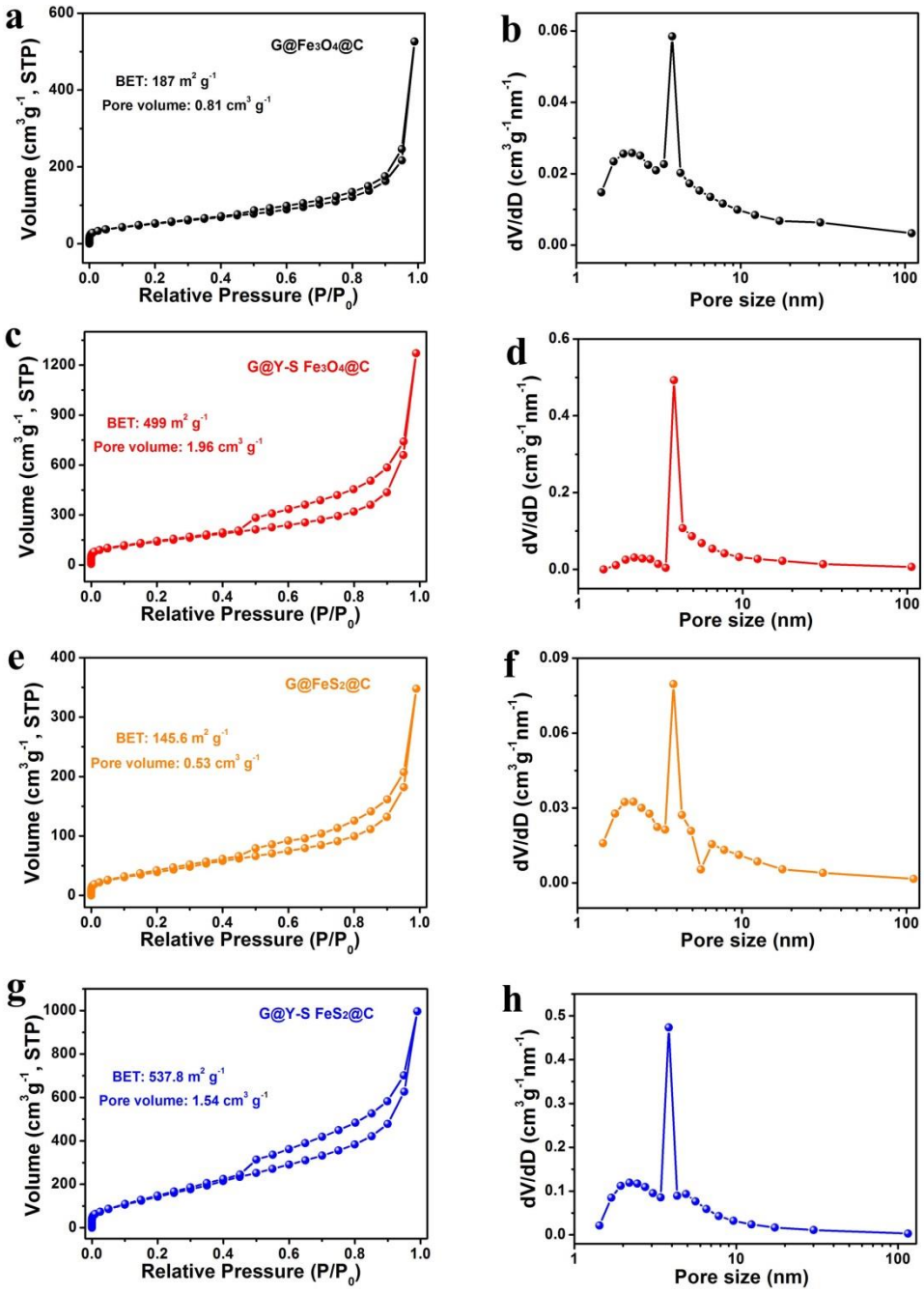

Figure S10. (a, c, e, g) Nitrogen absorption-desorption isotherms, and (b, d, f, h) pore size distribution of (a-b) G@Fe_3O_4@C, (c-d) G@Y-S Fe_3O_4@C, (e-f) G@FeS_2@C, and (g-h) G@Y-S FeS_2@C composites.

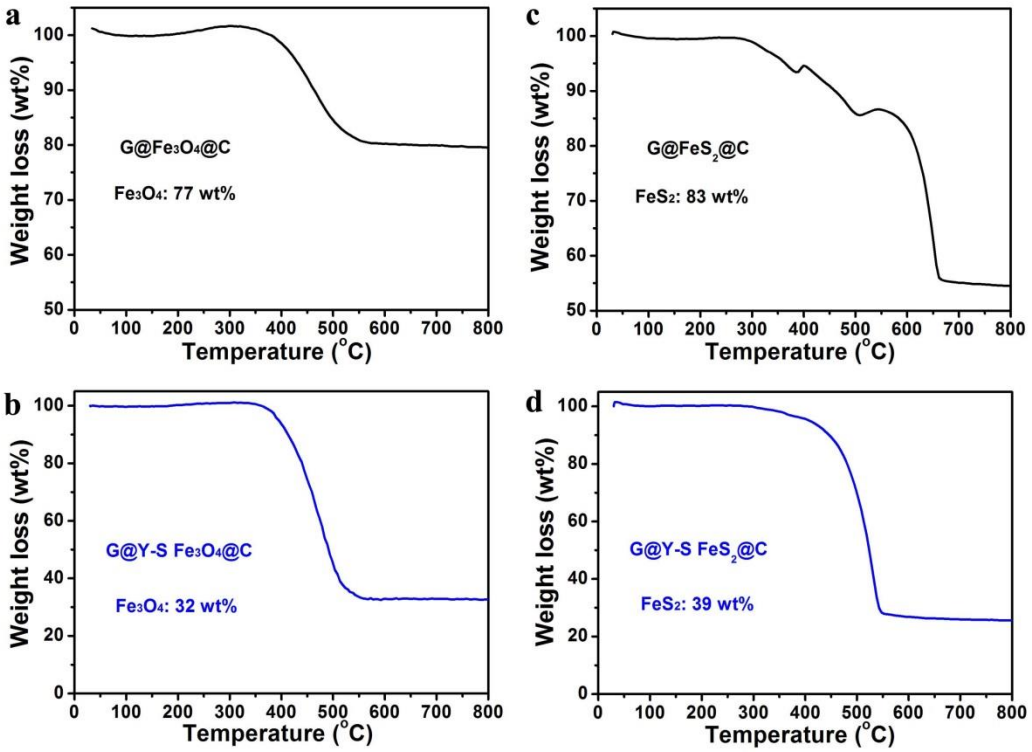

Figure S11. TGA curves of (a) G@Fe_3O_4@C, (b) G@Y-S Fe_3O_4, (c) G@FeS_2@C, and G@Y-S FeS_2@C composites.

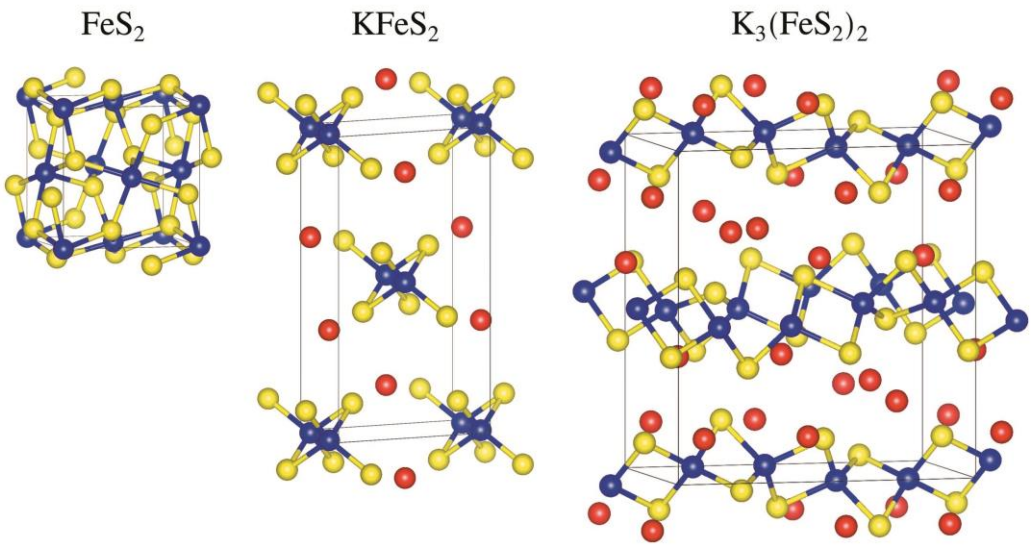

Figure S12. Crystal structures of FeS_2, $KFeS_2$, and $K_3(FeS_2)_2$. The Fe, S, and K atoms are shown in blue, yellow, and red color.

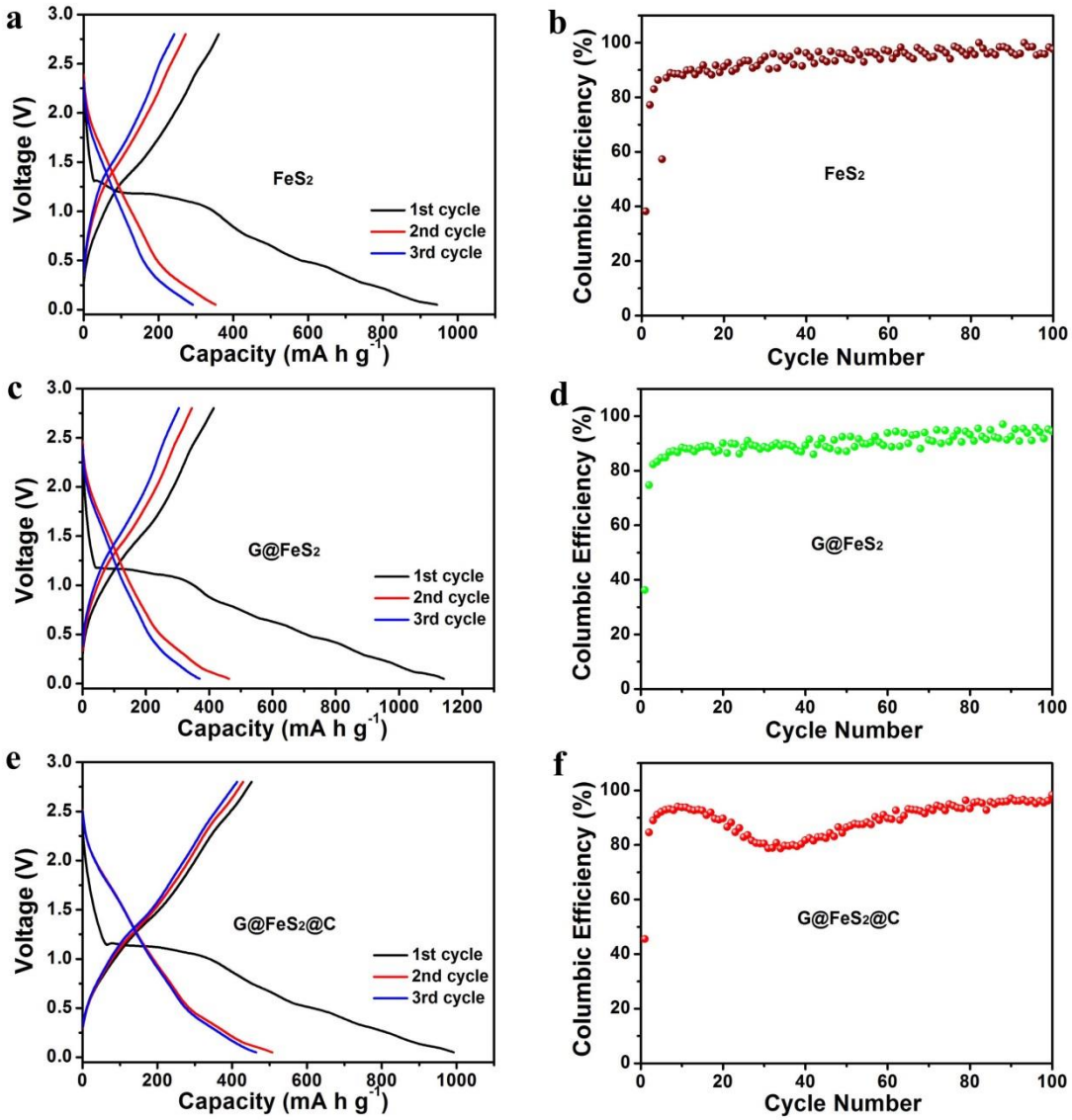

Figure S13. (a, c, e) Initial three discharge-charge curves, and (b, d, f) columbic efficiencies of (a-b) pure FeS_2, (c-d) G@FeS_2, and (e-f) G@FeS_2@C composites at a current density of 300 mA g^{-1}.

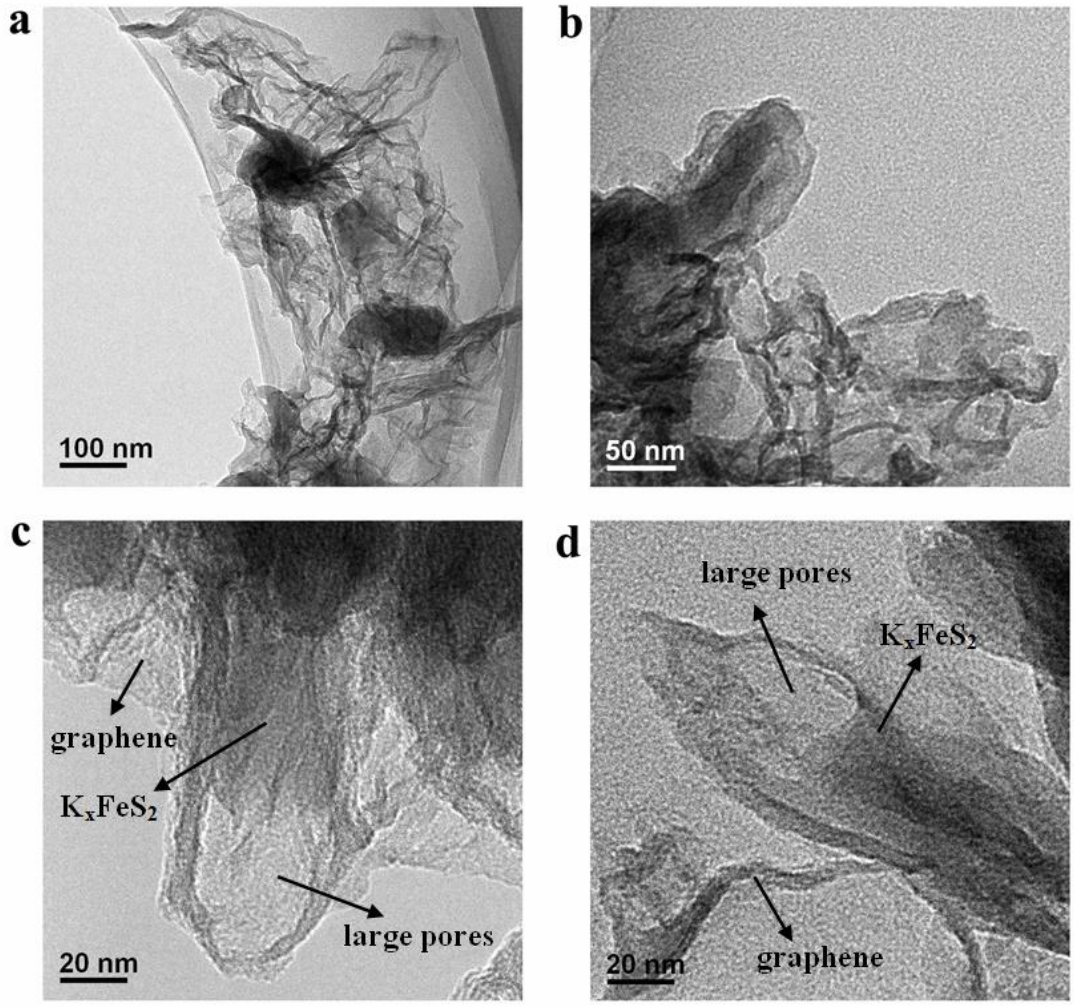

Figure S14. TEM images of G@Y-S FeS_2@C electrode after inital discharge/charge cycle.

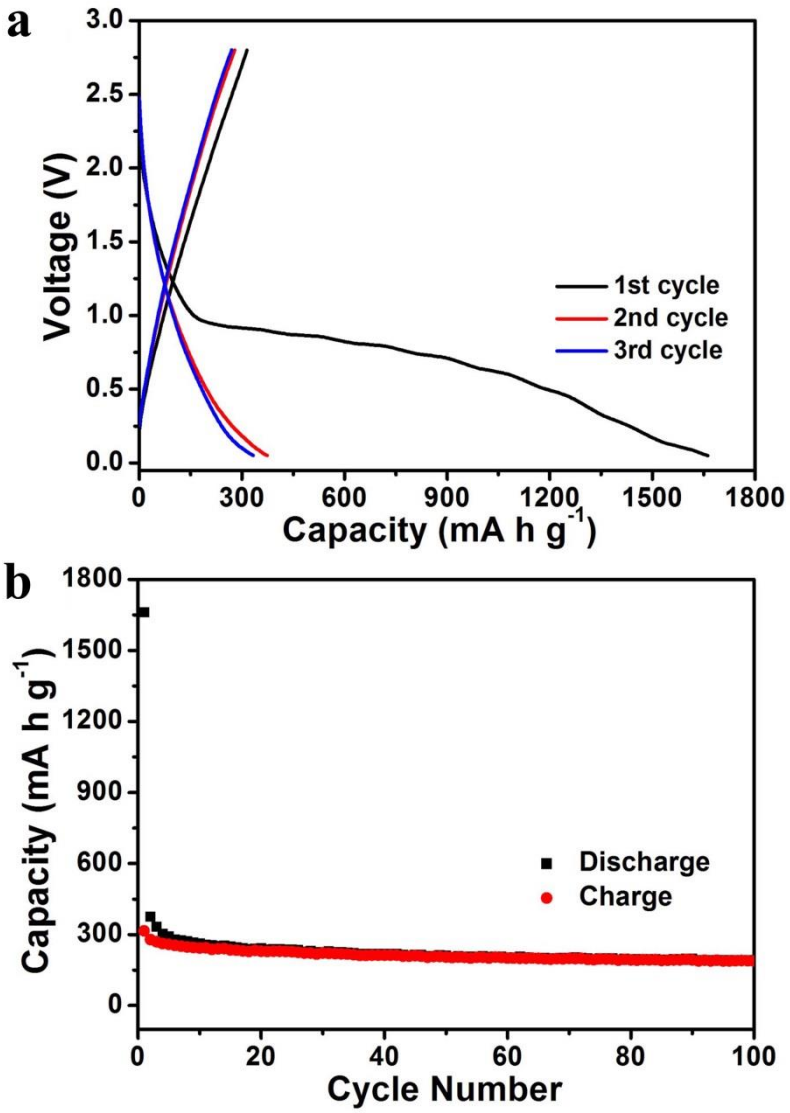

Figure S15. (a) Initial three discharge/charge profiles, and (b) cycling performance of G@hollow carbon electrode at a current density of 300 mA g^{-1}.

Table. S1 Comparison of as-reported anode materials for potassium ion batteries.

Materials	Current density (mA g^{-1})	**Cycle Number**	Capacity (mAh g^{-1})	Ref
Graphite	140	**50**	100	[1]
F-doped graphene	500	**200**	166	[2]
Graphite	20	**200**	220	[3]
Mesoporous Carbon	50/1000	**100/1000**	250/146	[4]
Carbon nanofiber	200	**1200**	211	[5]
P, O-dopd graphene	2000	**600**	160	[6]
Semi-hollow microrods	500	**500**	172	[7]
N-doped carbon monolith	20/500	**60/1000**	351/150	[8]
N-doped carbon nanotube	50/2000	**300/500**	254/102	[9]
N, O-doped hard carbon	50/1050	**100/1100**	230/125	[10]
SnS_2-graphene	25	**30**	250	[11]
Sn-C	25	**30**	110	[12]
VS_2 nanosheets	100/500	**60/100**	410/360	[13]
Black phosphorus-C	50	**50**	270	[14]
Co_3O_4–Fe_2O_3/C	50	**50**	220	[15]
Sb_2S_3/S, N-doped graphene	50	**100**	480	[16]
MoS_2 nanorose	100	**100**	380	[17]
CoS-graphene	500	**100**	310	[18]
Sn_4P_3/C	50	**50**	307	[19]
ReS_2/N-doped CNF	50	**100**	253	[20]
G@Y-S FeS_2@C	300	**100/1000**	308/270	**This work**
	1000	**1000**	161	
	2000	**1500**	122	
	5000	**1500**	100	

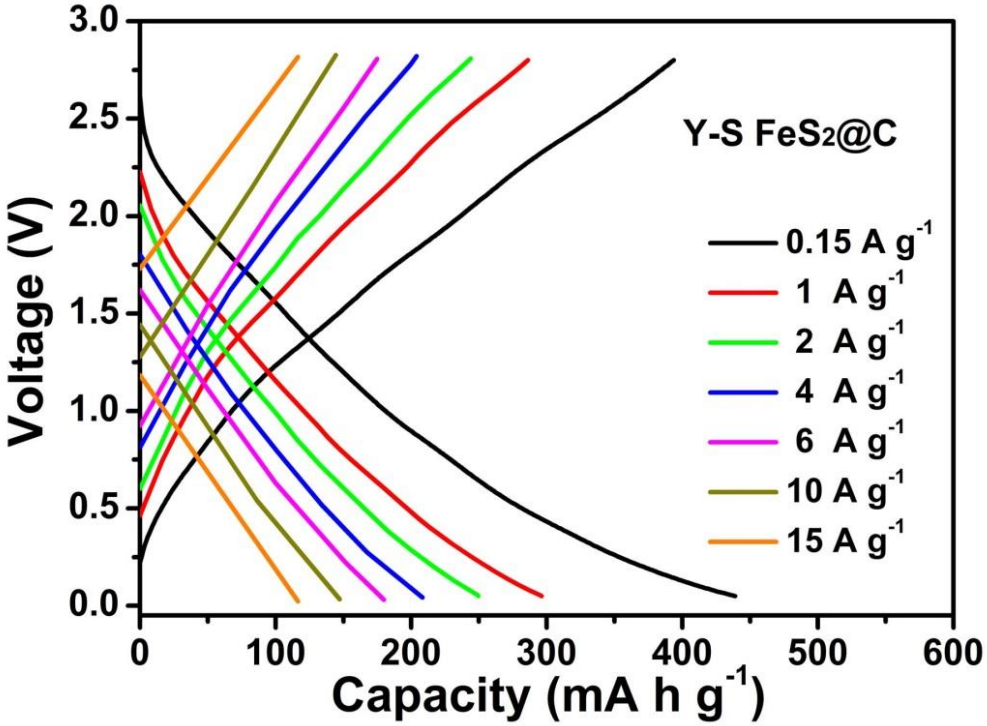

Figure S16. Typical discharge and charge profiles of Y-S FeS_2@C electrode under various rates from 0.15 to 15 A g^{-1}.

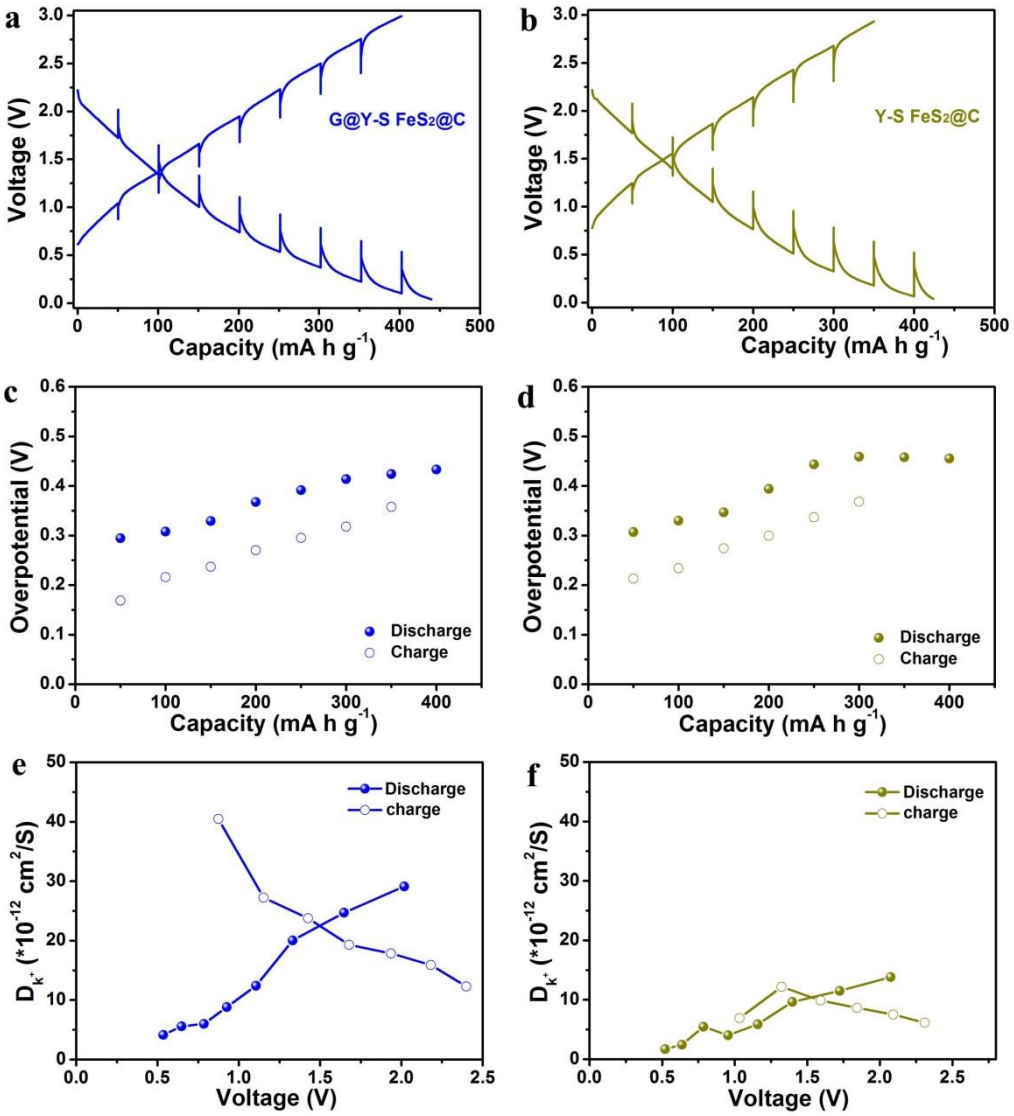

Figure S17. Galvanostatic intermittent titration technique (GITT) curves (a-b), derived overpotentials (c-d), and calculated K-ion diffusion coefficients (e-f) of G@Y-S FeS_2@C (a, c, e) and Y-S FeS_2@C (b, d, f) electrodes at 9th cycle. Data was recorded with a series of current pulses at 150 mA g^{-1} for 20 min and 4 h relaxation at each interval.

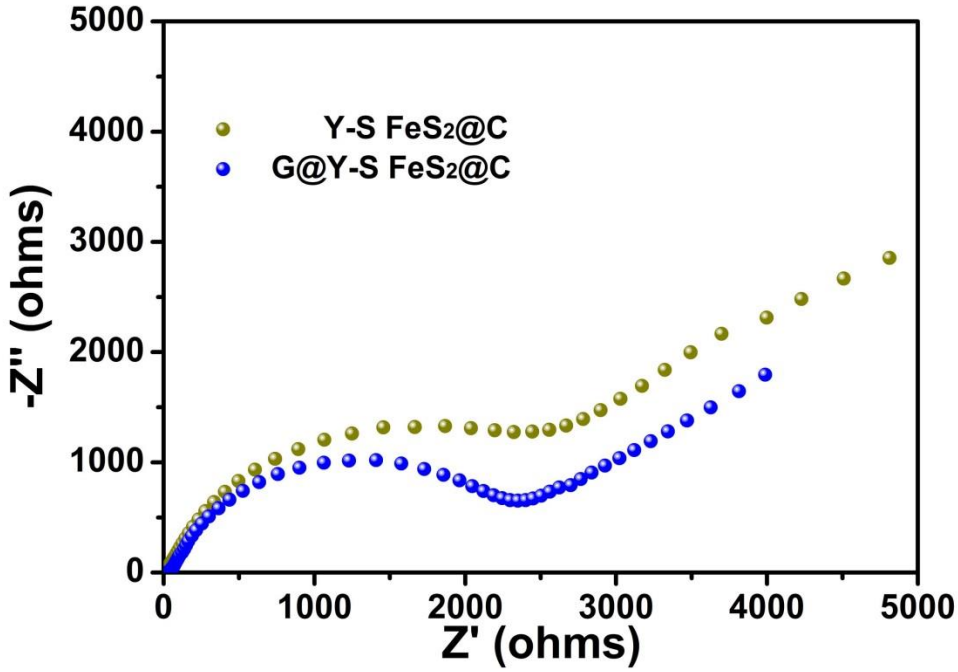

Figure S18. The electrochemical impedance spectroscopy (EIS) profiles of G@Y-S FeS_2@C and Y-S FeS_2@C electrodes after potassiation/depotassiation cycles.

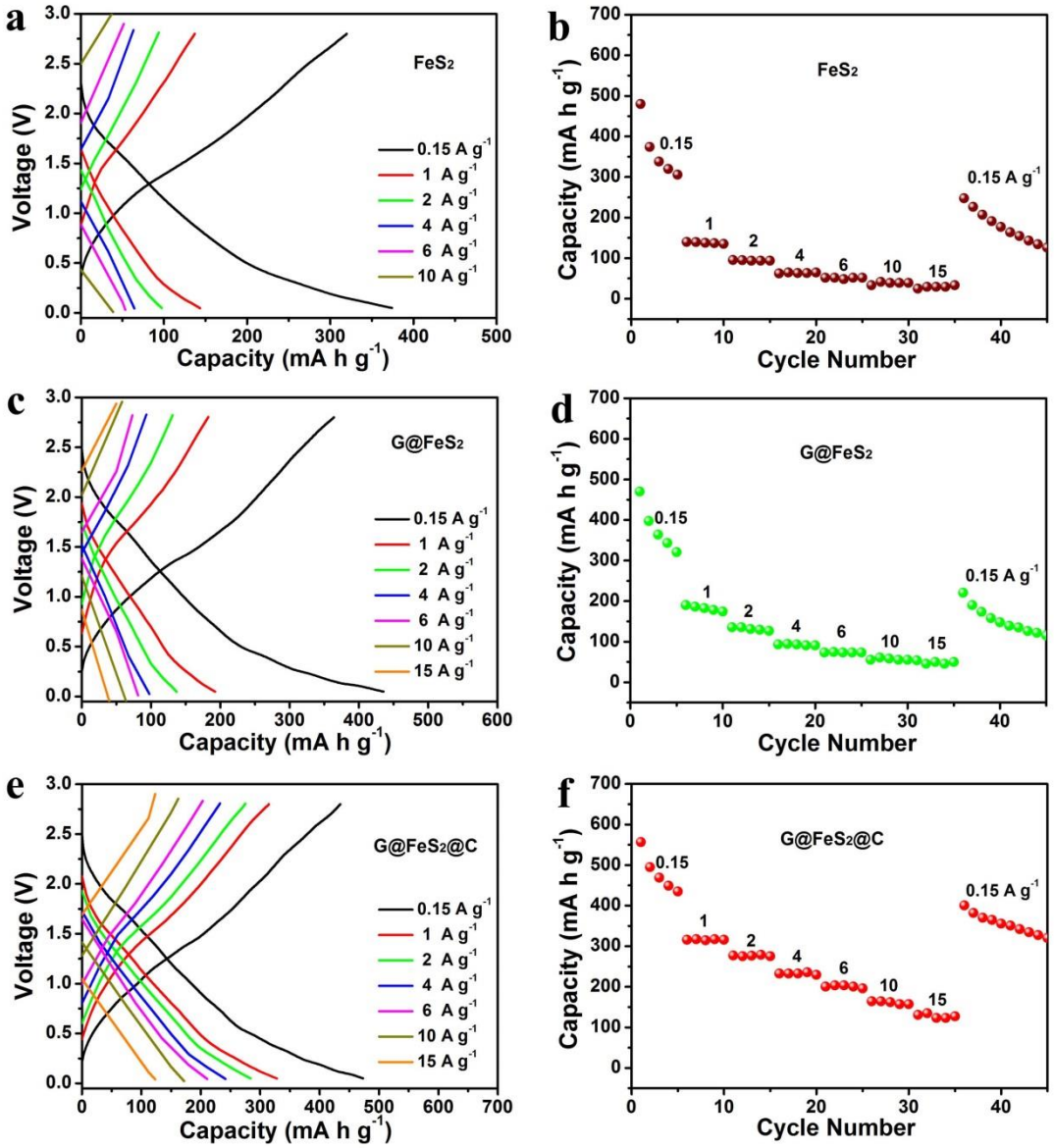

Figure S19. (a, c, e) Typical discharge/charge profiles, and (b, d, f) rate capabilities of (a-b) FeS_2, (c-d) G@FeS_2, and (e-f) G@FeS_2@C electrodes under various rates from 0.15 to 15 A g^{-1}.

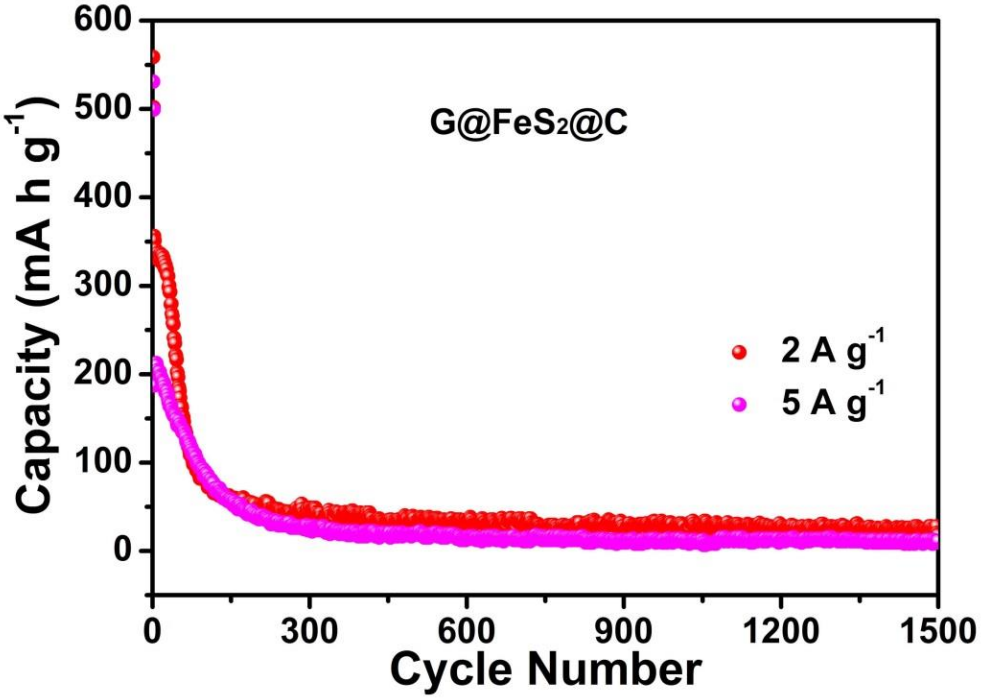

Figure 20. Long-term cycling stability of G@FeS_2@C electrode at high current densities of 2 and 5 A g^{-1} after being cycled at 0.15 A g^{-1} in the initial two cycles.

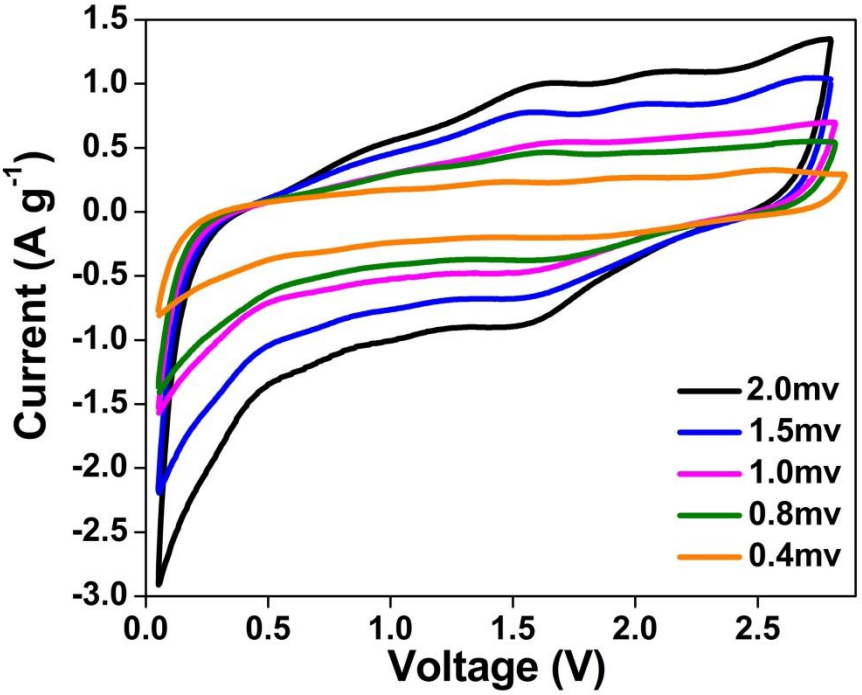

Figure S21. CV profiles of G@Y-S FeS_2@C electrode under various scan rates.

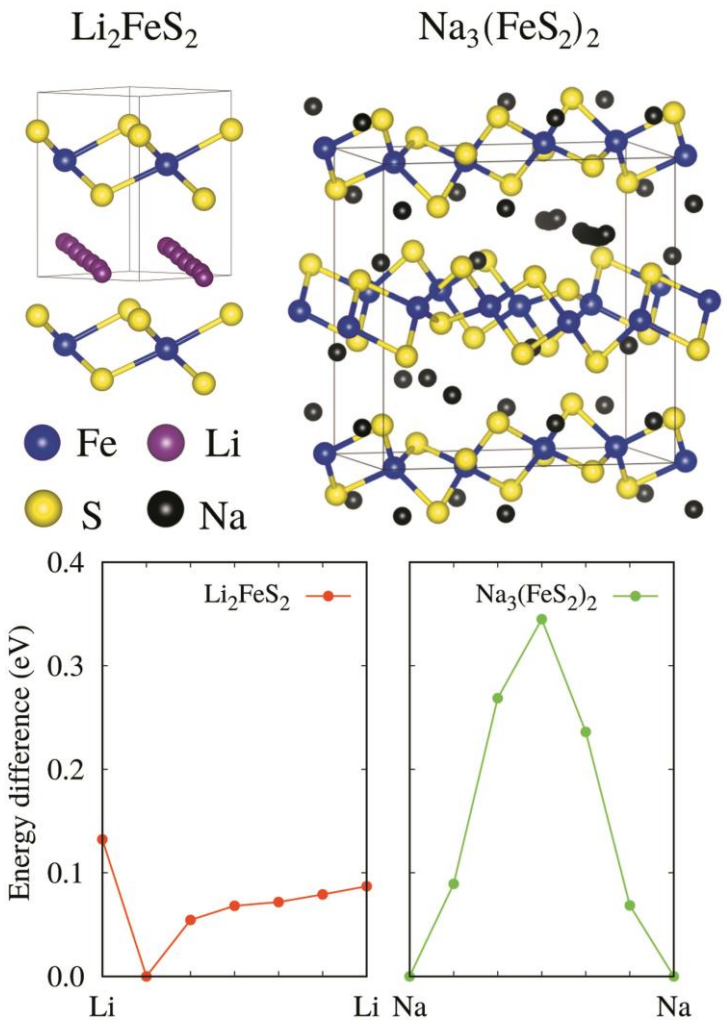

Figure S22. Paths and energy barriers for Li and Na diffusion in Li_2FeS_2 and $Na_3(FeS_2)_2$, respectively. The Fe, S, Li, and Na atoms are shown in blue, yellow, purple, and black color.

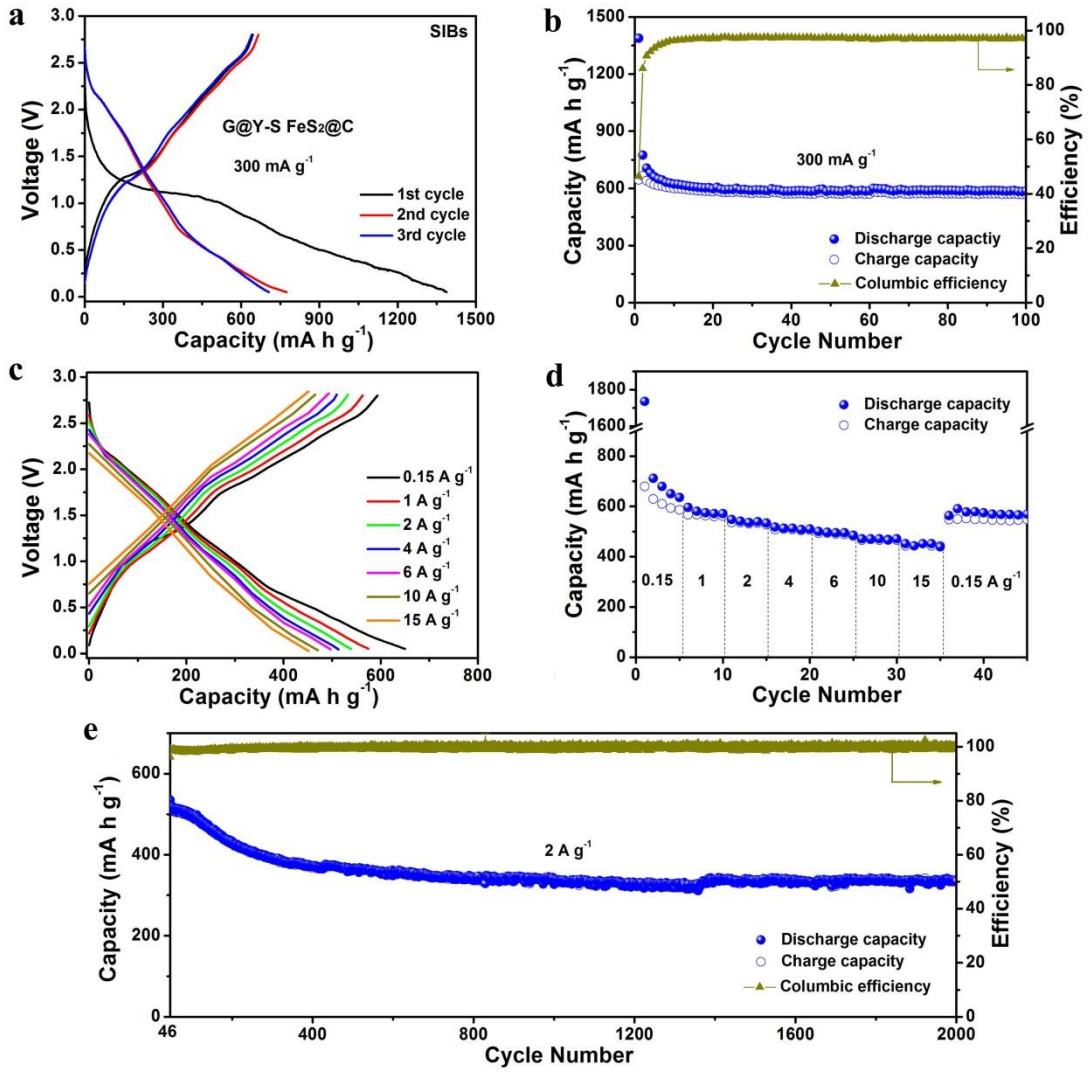

Figure S23. Sodium storage performance of G@Y-S FeS_2@C anode for SIBs. (a) Discharge and charge profiles of the initial three cycles, and (b) cycling performance at 300 mA h g^{-1}. (c) discharge/charge curves under various rates, and (d) rate capabilities from 0.15 to 15 A g^{-1}. (e) Long-term cycling stability at a high rate of 2 A g^{-1}.

Table. S2 Comparison of as-reported FeS_x anodes for sodium ion batteries.

Materials	Current density (A g^{-1})	Cycle Number	Capacity (mAh g^{-1})	Rate capability (mAh g^{-1}/A g^{-1})	Cut-off voltage	Ref
FeS_2 particles	0.2	800	524	323/5	0.5-3.0	[21]
Greigite Fe_3S_4	5/20	1000/3500	435/275	233/40	0.5-3.0	[22]
FeS@C	0.09/0.7	50/200	430/140	280/4.5	0.5-3.0	[23]
FeS_2@rGO	0.45	250	240	193/1.8	0.8-3.0	[24]
	0.45	100	150	-	0.1-3.0	
FeS_2/rGO aerogel	0.9	800	181	195/4.5	0.8-2.8	[25]
FeS_2/CNT network	0.1/1	400/1800	394/309	-	0.8-3.0	[26]
FeS_2 nanocyrstal	1	600	410	-	0.02-2.5	[27]
Yolk-shell FeS@C	0.1/1	100/100	618/560	275/10	0.05-3.0	[28]
FeS@rGO	0.15	50	547	367/5	0.001-3	[29]
C/FeS microsphere	1	200	300	65/5	0.01-3.0	[30]
FeS_x@C	0.1	100	636	403/2	0-2.5	[31]
$Fe_{1-x}S$	0.1/1	200/2000	536/475	300/10	0.005-3	[32]
FeS nanofiber	0.5	500	592	353/5	0.001-3	[33]
Ultrafine Fe_7S_8@C	0.18	1000	447	552/2.7	0.08-3.0	[34]
FeS_2@rGO	0.1	100	609	344/10	0.01-2.3	[35]
Yolk-shell FeS_2@C	0.1/2	100/800	511/330	403/5	0.2-2.0	[36]
G@Y-S FeS_2@C	**0.3/2**	**100/2000**	**568/336**	**451/15**	**0.05-2.8**	**This work**

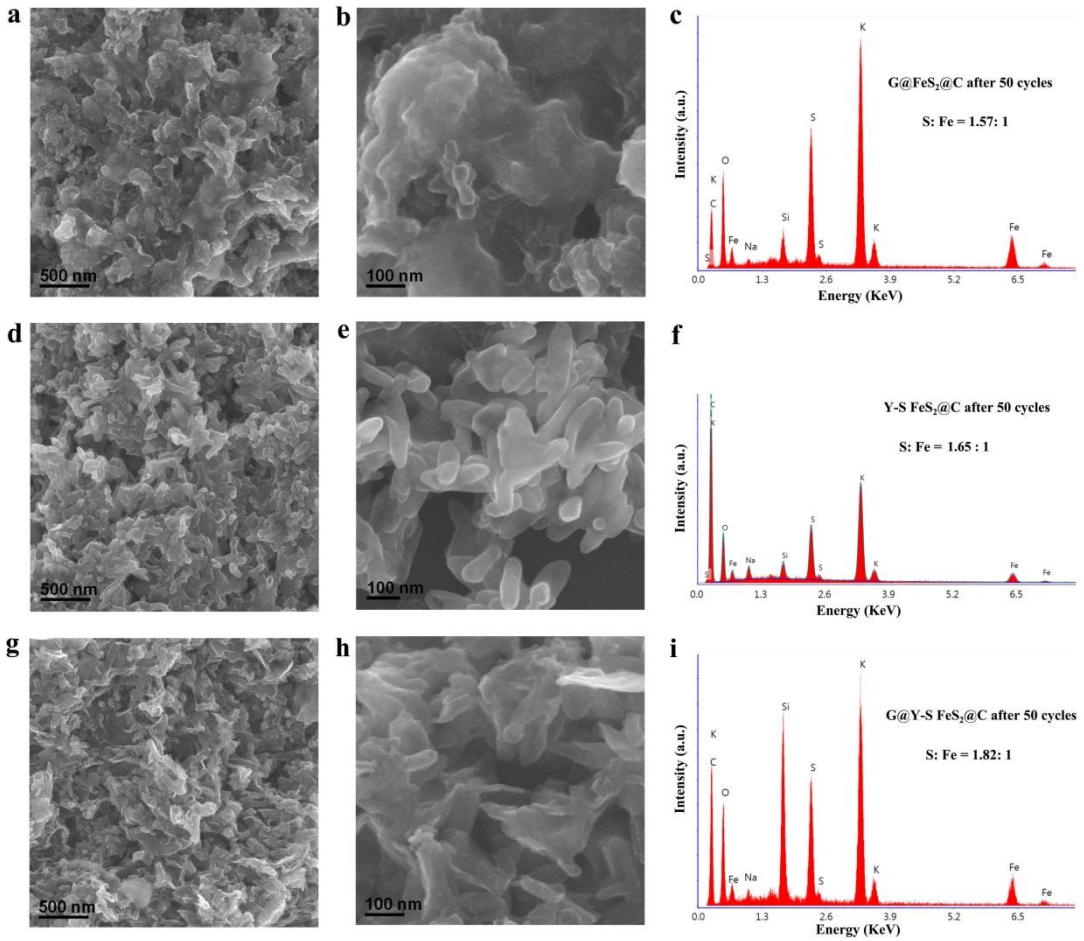

Figure S24. (a-b, d-e, g-h) SEM images, and (c, f, i) energy dispersive spectroscopy (EDS) patterns of (a-c) G@FeS_2@C, (d-f) Y-S FeS_2@C, and (g-i) G@Y-S FeS_2@C electrodes after 50 potassiation/depotassiation cycles.

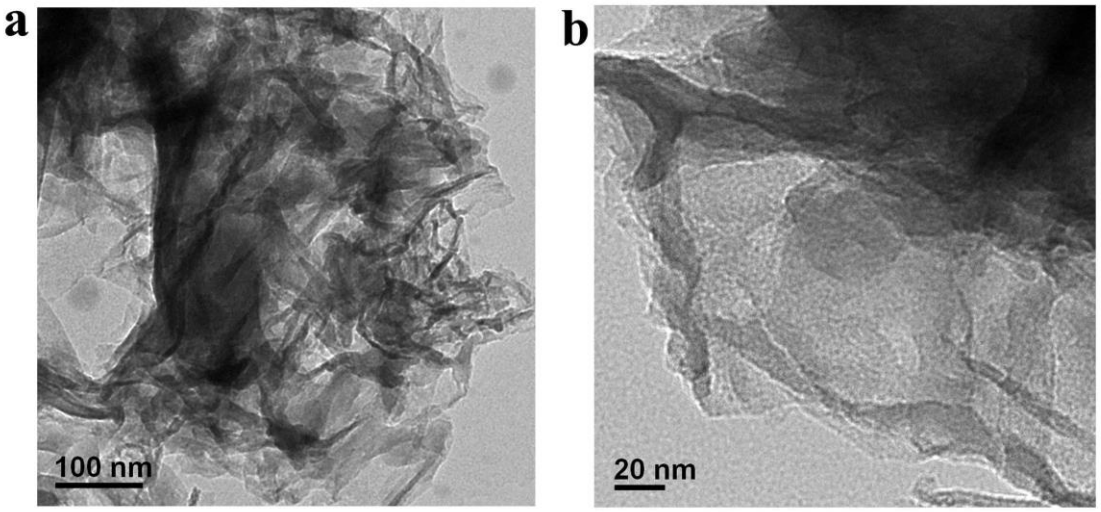

Figure S25. TEM images of G@Y-S FeS_2@C electrode after potassiation/depotassiation cycles.

Reference:

1. Z. L. Jian, W. Luo and X. L. Ji, *J. Am. Chem. Soc.*, **2015**, *137*, 11566.
2. Z. C. Ju, S. Zhang, Z. Xing, Q. C. Zhuang, Y. H. Qiang and Y. T. Qian, *ACS Appl. Mater. Inter.*, **2016**, *8*, 20682.
3. J. Zhao, X. X. Zou, Y. J. Zhu, Y. H. Xu and C. S. Wang, *Adv. Funct. Mater.*, **2016**, *26*, 8103.
4. W. Wang, J. H. Zhou, Z. P. Wang, L. Y. Zhao, P. H. Li, Y. Yang, C. Yang, H. X. Huang and S. J. Guo, *Adv. Energy Mater.*, **2018**, *8*, 1701648.
5. X. X. Zhao, P. X. Xiong, J. F. Meng, Y. Q. Liang, J. W. Wang and Y. H. Xu, *J. Mater. Chem. A*, **2017**, *5*, 19237.
6. G. Y. Ma, K. S. Huang, J. S. Ma, Z. C. Ju, Z. Xing and Q. C. Zhuang, *J. Mater. Chem. A*, **2017**, *5*, 7854.
7. X. P. Wang, K. Han, D. D. Qin, Q. Li, C. Y. Wang, C. J. Niu and L. Q. Mai, *Nanoscale*, **2017**, *9*, 18216.
8. Y. H. Xie, Y. Chen, L. Liu, P. Tao, M. P. Fan, N. Xu, X. W. Shen and C. L. Yan, *Adv. Mater.*, **2017**, *29*, 1702268.
9. P. X. Xiong, X. X. Zhao and Y. H. Xu, *Chemsuschem*, **2018**, *11*, 202.
10. J. L. Yang, Z. C. Ju, Y. Jiang, Z. Xing, B. J. Xi, J. K. Feng and S. L. Xiong, *Adv. Mater.*, **2018**, *30*, 1700104.
11. V. Lakshmi, Y. Chen, A. A. Mikhaylov, A. G. Medvedev, I. Sultana, M. M. Rahman, O. Lev, P. V. Prikhodchenko and A. M. Glushenkov, *Chem. Commun.*, **2017**, *53*, 8272.
12. I. Sultana, T. Ramireddy, M. M. Rahman, Y. Chen and A. M. Glushenkov, *Chem. Commun.*, **2016**, *52*, 9279.
13. J. H. Zhou, L. Wang, M. Y. Yang, J. H. Wu, F. J. Chen, W. J. Huang, N. Han, H. L. Ye, F. P. Zhao, Y. Y. Li and Y. G. Li, *Adv. Mater.*, **2017**, *29*, 1702061.
14. I. Sultana, M. M. Rahman, T. Ramireddy, Y. Chen and A. M. Glushenkov, *J. Mater. Chem. A*, **2017**, *5*, 23506.
15. I. Sultana, M. M. Rahman, S. Mateti, V. G. Ahmadabadi, A. M. Glushenkov and Y. Chen, *Nanoscale*, **2017**, *9*, 3646.
16. Y. Y. Lu and J. Chen, *Sci. China Chem.*, **2017**, *60*, 1533.
17. K. Y. Xie, K. Yuan, X. Li, W. Lu, C. Shen, C. L. Liang, R. Vajtai, P. Ajayan and B. Q. Wei, *Small*, **2017**, *13*, 1701471.
18. H. Gao, T. F. Zhou, Y. Zheng, Q. Zhang, Y. Q. Liu, J. Chen, H. K. Liu and Z. P. Guo, *Adv. Funct. Mater.*, **2017**, *27*, 1702634.

19. W. C. Zhang, J. F. Mao, S. A. Li, Z. X. Chen and Z. P. Guo, *J. Am. Chem. Soc*, **2017**, *139*, 3316.
20. M. L. Mao, C. Y. Cui, M. G. Wu, M. Zhang, T. Gao, X. L. Fan, J. Chen, T. H. Wang, J. M. Ma and C. S. Wang, *Nano Energy*, **2018**, *45*, 346.
21. K. Y. Chen, W. X. Zhang, L. H. Xue, W. L. Chen, X. H. Xiang, M. Wan and Y. H. Huang, *ACS Appl. Mater. Inter.*, **2017**, *9*, 1536.
22. Q. D. Li, Q. L. Wei, W. B. Zuo, L. Huang, W. Luo, Q. Y. An, V. O. Pelenovich, L. Q. Mai and Q. J. Zhang, *Chem. Sci.*, **2017**, *8*, 160.
23. X. Wei, W. H. Li, J. A. Shi, L. Gu and Y. Yu, *ACS Appl. Mater. Inter.*, **2015**, *7*, 27804.
24. W. H. Chen, S. H. Qi, M. M. Yu, X. M. Feng, S. Z. Cui, J. M. Zhang and L. W. Mi, *Electrochim Acta*, **2017**, *230*, 1.
25. W. H. Chen, S. H. Qi, L. Q. Guan, C. T. Liu, S. Z. Cui, C. Y. Shen and L. W. Mi, *J. Mater. Chem. A*, **2017**, *5*, 5332.
26. Y. Y. Chen, X. D. Hu, B. Evanko, X. H. Sun, X. Li, T. Y. Hou, S. Cai, C. M. Zheng, W. B. Hu and G. D. Stucky, *Nano Energy*, **2018**, *46*, 117.
27. M. Walter, T. Zund and M. V. Kovalenko, *Nanoscale*, **2015**, *7*, 9158.
28. Y. X. Wang, J. P. Yang, S. L. Chou, H. K. Liu, W. X. Zhang, D. Y. Zhao and S. X. Dou, *Nat. Commun.*, **2015**, *6*, 8689.
29. S. Y. Lee and Y. C. Kang, *Chem. Eur. J.*, **2016**, *22*, 2769.
30. Z. J. Cao, H. H. Song, B. Cao, J. Ma, X. H. Chen, J. S. Zhou and Z. K. Ma, *J. Power Sources*, **2017**, *364*, 208.
31. Y. Z. Tan, K. W. Wong, Z. L. Zhang and K. M. Ng, *Nanoscale*, **2017**, *9*, 19408.
32. L. L. Li, S. J. Peng, N. Bucher, H. Y. Chen, N. Shen, A. Nagasubramanian, E. Eldho, S. Hartung, S. Ramakrishna and M. Srinivasan, *Nano Energy*, **2017**, *37*, 81.
33. J. S. Cho, J. S. Park and Y. C. Kang, *Nano Res.*, **2017**, *10*, 897.
34. M. J. Choi, J. Kim, J. K. Yoo, S. Yim, J. Jeon and Y. S. Jung, *Small*, **2018**, *14*.
35. Q. H. Wang, C. Guo, Y. X. Zhu, J. P. He and H. Q. Wang, *Nano-Micro Lett.*, **2018**, *10*.
36. Z. M. Liu, T. C. Lu, T. Song, X. Y. Yu, X. W. Lou and U. Paik, *Energy Environ. Sci.*, **2017**, *10*, 1576.